AN ABSTRACT OF THE DISSERTATION OF

Samuel M. Kelly for the degree of Doctor of Philosophy in Oceanography presented on
December 6, 2010.

Title: Tide-Topography Coupling on a Continental Slope

Abstract approved: _____

Jonathan D. Nash

Tide-topography coupling is important for understanding surface-tide energy loss, the
intermittency of internal tides, and the cascade of internal-tide energy from large to small
scales. Although tide-topography coupling has been observed and modeled for 50 years,
the identification of surface and internal tides over arbitrary topography has not been
standardized. Here, we begin by examining five surface/internal-tide decompositions and
find that only one is (i) consistent with the normal-mode description of tides over a flat
bottom, (ii) produces a physically meaningful depth-structure of internal-tide energy flux,
and (iii) results in an established expression for internal-tide generation. Next, we examine
the expression for internal-tide generation and identify how it is influenced by remotely-
generated shoaling internal tides. We show that internal-tide generation is subject to both
resonance and intermittency, and can not always be predicted from isolated regional models.
Lastly, we quantify internal-tide generation and scattering on the Oregon Continental slope.
First, we derive a previously unpublished expression for inter-modal energy conversion.
Then we evaluate it using observations and numerical simulations. We find that the
surface tide generates internal tides, which propagate offshore; while at the same time,
low-mode internal tides shoal on the slope, scatter, and drive turbulent mixing. These

results suggest that internal tides are unlikely to survive reflection from continental slopes, and that continental margins play an important role in deep-ocean tidal-energy dissipation.

Tide-Topography Coupling on a Continental Slope

by

Samuel M. Kelly

A DISSERTATION

submitted to

Oregon State University

in partial fulfillment of
the requirements for the
degree of

Doctor of Philosophy

Presented December 6, 2010
Commencement June 2011

Doctor of Philosophy dissertation of Samuel M. Kelly presented on December 6, 2010.

APPROVED:

_____

Major Professor, representing Oceanography

_____

Dean of the College of Oceanic and Atmospheric Sciences

_____

Dean of the Graduate School

ACKNOWLEDGEMENTS

CONTRIBUTION OF AUTHORS

Dr. Eric Kunze coauthored chapters 2 and 4. Dr. Kim I. Martini and Dr. Matthew H. Alford coauthored chapter 4. In all instances coauthors contributed through data collection, analysis, and writing

TABLE OF CONTENTS

LIST OF FIGURES

LIST OF FIGURES (Continued)

LIST OF TABLES

DEDICATION

To my wife, brother, and parents.

1. INTRODUCTION

"In such a stratified medium the phenomena of the tides express themselves in another fashion, namely as great submarine waves in the boundary surfaces between the layers of water." - Otto Pettersson (1931)

The periodic rise and fall of the sea is intertwined in the human experience. Human's have been observing and predicting tides for thousands of years (*Cartwright*, 1999). Therefore, it is unsurprising that tides have been scientifically described for hundreds of years. One of Newton's triumphs in the *Principia* (1687) was to explain the astronomical tide-generating force (*Hendershott*, 1981). A century later, in 1776, Laplace presented the general equations for tidal motion. At this time, describing tides with better accuracy seemed to be as straightforward as improving observations and computations. However, in the early 1900's, technological advances, such as the invention of the Nansen-Pettersson bottle, facilitated the first detailed measurements of subsurface temperature and salinity. *Nansen* (1902) and *Helland-Hansen and Nansen* (1909) observed oceanic internal waves during expeditions in the arctic, but could not determine their frequency. In 1907, *Pettersson* discovered internal tides (internal waves with tidal frequency) in observations from the Great Belt.

The discovery of internal tides ended the 150-year-old approximation that tides are unaffected by stratification. By the 1940's Laplace's tidal equations had been extended to include stratification (*Hendershott*, 1981). However, rewriting the tidal equations did little to answer the most basic of questions, such as: How are internal tides generated? How can we predict internal tides? and How are internal tides dissipated? One hundred years after the discovery of internal tides, these basic questions remain largely unanswered. In this

dissertation, we address aspects of these questions using theory, numerical simulations, and observations. Chapter 2 decomposes motion into surface and internal tides and mathematically describes the origin of tidal coupling over topography. Chapter 4 examines time variability in internal-tide generation and suggests it may be intermittent, bringing to light new challenges for predicting internal tides. Chapter 5 examines the cascade of tidal energy on the Oregon continental slope, providing evidence that continental margins are a source of deep-ocean tidal dissipation.

1.1   Why Do Internal Tides Exist?

"In the baldest terms, it has always been difficult to understand why such waves existed"
-Carl Wunsch (1975)

Shortly after the discovery of internal tides, *Zeilon* (1912) demonstrated their generation over topography in laboratory experiments. Despite this discovery, over the next 50 years, many studies attempted to explain internal-tide generation using the astronomical tide-generating force directly (e.g., *Pettersson*, 1930). It was not until *Rattray* (1960) and *Cox and Sandstrom* (1962) that a mathematical description of topographic internal-tide generation was published. Shortly afterward, tide-topgraphy coupling became the accepted mechanism for internal-tide generation (*Munk*, 1966, 1968; *Wunsch*, 1975). Using a numerical model, *Jayne and St. Laurent* (2001) confirmed the importance of topographic internal-tide generation by showing that deep-ocean satellite observations of surface-tide energy loss (*Egbert and Ray*, 2000) coincide with large internal-wave drag.

Early models of internal-tide generation contained idealized topography and stratification, but employed different solution strategies. *Rattray* (1960) introduced

solutions using vertical modes that are still being developed for idealized (e.g., *St. Laurent et al.*, 2003) and arbitrary (e.g., *Griffiths and Grimshaw*, 2007) topography. *Baines* (1973, 1974, 1982), *Sandstrom* (1976), and *Craig* (1987) developed solutions using wave characteristics, but these are difficult to apply in three dimensions. *Bell* (1975a,b) produced an analytical solution for internal-tide generation over infinitesimal topography, which has subsequently been modified for more general topography (e.g., *Llewellyn Smith and Young*, 2002; *Nycander*, 2005). *Robinson* (1969) solved for internal-tide generation at a knife ridge using a Green's function. The Green's function solution has recently been extended to arbitrary topography (e.g., *Pétrélis et al.*, 2006; *Echeverri and Peacock*, 2010).

Although analytical solutions continue to be developed, the falling cost of computational resources has made numerical models the most accessible method for estimating internal-tide generation. These models are designed to approximate the Navier-Stokes equations with parameterized surface-tide forcing, making it straightforward to include advection, dissipation, arbitrary topography, and realistic stratification. *Chuang and Wang* (1981) appear to have presented the first two-dimensional simulation, *Holloway* (1996) and *Cummins and Oey* (1997) the first three-dimensional simulations, and *Simmons et al.* (2004) the first global simulation of internal-tide generation. In the last decade, dozens of studies have conducted three-dimensional simulations of internal-tide generation. This explosion can be attributed to renewed interest in internal tides (e.g., *Munk and Wunsch*, 1998), the availability of computational resources, and the accessibility of "community" general circulation models (e.g., *Marshall et al.*, 1997; *Shchepetkin and McWilliams*, 2005).

Simulating internal tides with brute computation has not guided us directly towards a clearer understanding of internal-tide generation. For instance, to compare estimates of internal-tide generation, we must uniformly define surface and internal tides. Unfortunately, in the last decade, modeling and observational studies have employed numerous conflicting

definitions over sloping topography: (i) *Baines* (1982) suggested that surface tides could be obtained from unstratified simulations, (ii) *Lu et al.* (2001) suggested that surface tides should include isopycnals heaved by surface-tide velocities at sloping topography, (iii) *Kunze et al.* (2002) suggested the equivalent of a normal-mode decomposition, which is now widely used by the oceanographic community, and (iv) *Gerkema and van Haren* (2007) suggested that internal-tide pressure gradients should include wave drag, contradicting the decomposition of *Kunze et al.* (2002). In Chapters 2 and 3, we review and compare these surface/internal-tide decompositions. To assess the merits of each decomposition, we examine their consistency with "flat-bottom" normal modes, depth-structure of internal-tide energy flux, and expressions for internal-tide generation. The conclusions of these chapters propose a simple surface/internal-tide decomposition (closely related to *Kunze et al.*, 2002) and clearly identify the general expression for topographic internal-tide generation. Standardizing these concepts allows for unambiguous comparisons between observational, analytical, and numerical estimates of internal tides and internal-tide generation.

1.2 How Can We Predict Internal Tides?

"Aside from ubiquity, and the at least quasi-tidal periodicity, the most common observation is that the internal tides tend to come and go, i.e., they appear to be intermittent.' -Carl Wunsch (1975)

Predictions of internal tides, like surface tides, are necessary for understanding a variety of processes. Internal tides affect abyssal stratification (e.g., *Munk and Wunsch*, 1998), influence acoustic transmission (e.g., *Dushaw*, 2006), produce across-shelf transport (e.g., *Shroyer et al.*, 2010), resuspend sediment (e.g., *Butman et al.*, 2006), shape continental

shelves (*Cacchione et al.*, 2002), drive ecological processes (e.g., *Pineda*, 1991; *Noble et al.*, 2009; *Sharples et al.*, 2009), endanger subsurface structures (e.g., *Osborne and Burch*, 1980), and "contaminate" measurements of the ocean's background stratification (e.g., *Nansen*, 1902). Unfortunately, internal tides, unlike surface tides, are difficult to predict because they are inexplicably intermittent (e.g., *Wunsch*, 1975).

Some intermittency in internal tides is explained by observations that they radiate thousands of kilometers from their place of generation (*Ray and Mitchum*, 1996; *Ray and Cartwright*, 2001; *Alford et al.*, 2007; *Zhao and Alford*, 2009; *Zhao et al.*, 2010). Near topographic features, observations of internal tides are likely to contain a superposition of locally and remotely-generated waves. The remotely-generated internal tide, which may have propagated for over a week, will have pseudo-random phase, direction, and amplitude, because these attributes are modified by the background stratification and velocity of the fluid through which they have transited (*Rainville and Pinkel*, 2006).

In the analysis of observations it is often necessary to consider the role of remotely-generated internal tides. Recently, we included these waves in a simulation of internal-tide generation. The results indicate that internal-tide energy, energy flux, and generation are sensitive to the amplitude and phase of the remotely-generated internal tide (Chapter 4). We conclude that internal-tide generation is itself intermittent and can not be predicted solely by local variables (i.e., topography, stratification, and surface tides). We also speculate that internal-tide generation is susceptible to resonance and could be chaotic. We suggest that in order for future regional internal-tide models to be first-order accurate, they will have to be coupled to global internal-tide models.

1.3 What Role Do Internal Tides Play in the Ocean Energy Balance?

"To many readers, the proposal that the Moon plays a major role in the general circulation will border on the lunatic." -Walter Munk and Carl Wunsch (1998)

It has long been known that motion in the ocean is forced by mechanical rather than thermal processes (*Sandström*, 1908; *Jeffreys*, 1926; *Wunsch and Ferrari*, 2004). The ocean is powered by 20 TW of wind and 3.5 TW of tides (*Munk and Wunsch*, 1998). Although surface winds are more energetic than tides, tides have the unique role of directly forcing the abyssal ocean. At first glance, these energy sources seem unlikely to drive ocean circulation because they occur at drastically different time and space scales than abyssal currents (i.e., tides have periods of hours, rather than thousands of years). However, winds and tides influence the general circulation through turbulent mixing, which alters abyssal stratification (e.g., *Munk*, 1966; *Munk and Wunsch*, 1998) and induces meridional transport (e.g., *Samelson*, 1998; *St. Laurent et al.*, 2001; *Nycander et al.*, 2007). Therefore, predicting the general circulation of the deep ocean relies on understanding the cascade of tidal energy from astronomical forcing to turbulent mixing.

In 1695, eight years after Newton explained the astronomical tide-generating force, Halley reported that ancient eclipses were inconsistent with the present Earth-Moon-Sun system (*Munk*, 1968). It was not until *Street* (1917), *Taylor* (1919), and *Jeffreys* (1920) that this inconsistency was correctly attributed to tidal-energy dissipation. However, these studies only considered the role of bottom friction in shallow seas. *Munk* (1966), applying the results of *Cox and Sandstrom* (1962), was the first to recognize the importance of internal-tide generation, estimating that this process could acount for 1/6 of surface-tide energy loss. Observations have since confirmed that internal-tide generation accounts for

0.7±0.15 TW (*Egbert and Ray*, 2000) out of 3.5 TW of total surface-tide energy loss (*Munk and Wunsch*, 1998).

Because existing internal tides can affect subsequent internal-tide generation (and even return energy to the surface tide, Chapter 4), internal-tide energy must be considered a part of the Earth-Moon-Sun energy balance until it is has been converted to heat by molecular viscosity (*Simmons et al.*, 2004). What is currently lacking is a global map of internal-tide dissipation. Owing to the long-range propagation of low-mode internal tides, it seems likely that such a map will be vastly different from current maps of internal-tide generation.

Understanding the dissipation of internal tides is fundamental to understanding the role of tidal energy in the ocean. Energy contained in internal tides can be redistributed to different frequencies and spatial scales through a variety of linear and nonlinear processes. Some processes involve critical layers (e.g., *Winters and Riley*, 1992), critical latitudes (e.g., *MacKinnon and Winters*, 2005), and/or a variety of wave-wave interactions (e.g., *Müller et al.*, 1986). Topographic reflection and scattering can also redistribute internal tide energy (e.g., *Johnston and Merrifield*, 2003) and produce turbulent mixing (e.g., *Gilbert and Garrett*, 1989), particularly over near-critical slopes (e.g., *Slinn and Riley*, 1998; *Gayen and Sarkar*, 2010).

An attractive aspect of tide-topography coupling is that low-mode scattering, like internal-tide generation, appears to be approximately linear. In Chapter 5 we examine observations of internal tides on the Oregon continental slope, a location of both internal-tide generation and scattering (*Nash et al.*, 2007; *Martini et al.*, 2011a,b). To quantify both processes, energy equations are decomposed for each vertical mode to obtain a previously unpublished expression for inter-modal energy conversion. Assuming that flow is uniform in the along-slope direction, we also apply a new method to resolve onshore and offshore-propagating internal tides. Our results indicate that internal tides are generated locally

and propagate offshore; while at the same time, remotely-generated internal tides shoal, scatter to higher modes, and drive local turbulent mixing (*Moum et al.*, 2002; *Nash et al.*, 2007; *Martini et al.*, 2011b). Chapter 5 closes by proposing that shoaling internal tides are unlikely to survive reflection from continental slopes, and that continental margins play an important role in deep-ocean tidal-energy dissipation.

2. INTERNAL-TIDE ENERGY OVER TOPOGRAPHY

Samuel M. Kelly, Jonathan D. Nash, and Eric Kunze

Abstract

The method used to separate surface and internal tides ultimately defines properties such as internal-tide generation and the depth-structure of internal-tide energy flux. Here, we provide a detailed analysis of several surface/internal-tide decompositions over arbitrary topography. In all decompositions, surface-tide velocity is expressed as the depth-average of total velocity. Analysis indicates that surface-tide pressure is best expressed as the depth-average of total pressure plus a new depth-dependent profile of pressure, which is due to isopycnal heaving by movement of the free surface. Internal-tide velocity and pressure are defined as total variables minus the surface-tide components. Corresponding surface- and internal-tide energy equations are derived that contain energy conversion solely through topographic internal-tide generation. The depth-structure of internal-tide energy flux produced by the new decomposition is unambiguous and differs from that of past decompositions. Numerical simulations over steep topography reveal that the decomposition is self-consistent and physically relevant. Analysis of observations over Kaena Ridge, Hawaii and the Oregon continental slope indicate $O(50 \text{ W m}^{-1})$ error in depth-integrated energy fluxes when internal-tide pressure is computed as the residual of pressure from its depth average (*Kunze et al.*, 2002). While these errors are small at major internal-tide generation sites, they may be significant where surface tides are larger and depth-integrated fluxes weaker (e.g., over continental shelves).

2.1 Introduction

Astronomical forcing of the ocean produces surface tides which propagate as shallow-water edge waves. When surface tides encounter topography, they deform and perturb

stratified fluid, generating internal tides. To obtain a meaningful expression of surface-to-internal-tide energy conversion, the surface and internal tides must be correctly identified. Deriving a relevant and practical method of isolating internal tides is an important step to understanding their physics.

Over a flat bottom, a simple method for identifying internal tides is normal-mode decomposition (e.g., *Wunsch*, 1975). This solution identifies the depth-structure and phase speed of internal tides, but does not provide an expression for topographic internal-tide generation, because it does not apply over a sloping bottom.

Baines (1982) suggested that internal tides could be identified over arbitrary topography by removing motion reproduced in an identical but unstratified fluid. *Niwa and Hibiya* (2001), *Khatiwala* (2003), and *Legg and Huijts* (2006) used this method to identify internal tides in numerical experiments. *Lu et al.* (2001) and *Di Lorenzo et al.* (2006) criticized this method for ignoring the effect of internal-wave drag on the surface tide. Additionally, interpreting oceanographic observations is not possible with this decomposition.

As a practical solution, *Kunze et al.* (2002) identified internal tides as the residuals of pressure and horizontal velocity after subtracting depth-averages. By default, this decomposition identifies surface tides as depth-averages of pressure perturbation and velocity. Conveniently, surface tides can vary by an unknown constant without altering the corresponding internal tides, allowing the decomposition to be applied to ocean observations and numerical simulations (e.g., *Kunze et al.*, 2002; *Alford*, 2003; *Althaus et al.*, 2003; *Simmons et al.*, 2004; *Nash et al.*, 2004, 2005; *Alford et al.*, 2006; *Nash et al.*, 2006; *Carter et al.*, 2006, 2008; *Duda and Rainville*, 2008). *Gerkema and van Haren* (2007) criticized this decomposition for being inconsistent over sloping topography. However, we dispute this assertion in Section 2.3.2. More importantly, *Kurapov et al.* (2003) found that this decomposition results in spurious surface-to-internal-tide energy conversion over both flat

and sloping topography. Here, we eliminate spurious conversion by removing pressure due to isopycnal heaving by movement of the free surface. *Lu et al.* (2001) made an analogous surface/internal-tide decomposition but also removed pressure due to isopycnal heaving by the surface tide flowing over topography. The decomposition of *Lu et al.* (2001) is examined here and found to provide unphysical distributions of surface-to-internal-tide conversion.

It is the purpose of this note to identify a complete, consistent, and practical method for identifying the internal tide. In Section 2.2, we begin deriving a surface/internal-tide decomposition which depends on an arbitrary profile of pressure. In Section 2.3, we examine five different methods of decomposing pressure. The first is that implied by *Baines* (1982), the second *Gerkema and van Haren* (2007), the third *Kunze et al.* (2002), and the fifth *Lu et al.* (2001). The fourth decomposition (Section 2.3.4) is similar to that of *Kunze et al.* (2002) but includes a correction to account for pressure due to isopycnal heaving by movement of the free surface. During this investigation, an emphasis is placed on the implications of each physical assumption. Careful examination of the momentum budget refutes objections raised by *Gerkema and van Haren* (2007), indicating that their derivation predetermines an alternative surface/internal-tide decomposition which is unphysical and incompatible with that of *Kunze et al.* (2002). In Section 2.4, numerical simulations and observations are used to examine the depth-structure of internal-tide energy flux and confirm the accuracy of the tidally-averaged internal-tide energy equations. The decomposition proposed here eliminates spurious energy conversion and provides the most physically-relevant description of internal-tide energetics. In Section 2.5, conclusions are presented.

2.2 Beginning a Decomposition

Although surface/internal-tide decompositions are routinely employed in oceanographic literature, they are rarely discussed and/or motivated in detail. Here, we develop several decompositions noting the physical implications of each assumption.

2.2.1 Requisites of a Decomposition

Before attempting to decompose flow, it is useful to define some requisites for success: (A) Completeness: the sum of the surface- and internal-tide should equal the total flow. (B) Consistency: surface- and internal-tide variables should reduce to normal-mode solutions over a flat bottom. (C) Practicality: the decomposition should be physically interpretable and applicable for interpreting observations and numerical simulations.

Requisite A discourages a complete decomposition using normal modes derived over a flat bottom because they require $w|_{z=-h} = 0$ so do not satisfy the boundary condition over sloping topography (Appendix). Requisite B precludes dynamically balanced modes (i.e. modes that do not contain topographic internal-tide generation) because energy fluxes over a flat bottom routinely identify steep topography as a source of internal-tide energy via the divergence theorem.

2.2.2   Total Equations of Motion

We start with linear, Boussinesq, f-plane, hydrostatic, momentum, continuity, and buoyancy equations:

$$u_t - fv = -p_x \tag{2.1}$$

$$v_t + fu = 0 \tag{2.2}$$

$$0 = -p_z + b \tag{2.3}$$

$$u_x + w_z = 0 \tag{2.4}$$

$$b_t + wN^2 = 0 \ , \tag{2.5}$$

where partial derivatives are denoted with subscripts. Buoyancy perturbation is $b = -g(\rho_{tot} - \bar{\rho}_{tot})/\rho_0$, where $(\bar{\cdot})$ denotes a time-average, ρ_{tot} total density and ρ_0 a constant reference density. p_{tot} is total pressure and $p = (p_{tot} - \bar{p}_{tot})/\rho_0$ pressure perturbation scaled by reference density (i.e., reduced pressure). $N^2(z)$ is the time-averaged buoyancy gradient (assumed to be horizontally uniform). For simplicity, uniformity is assumed in the y-direction, $(\cdot)_y = 0$.

The surface is located at $z = \eta$ and the bottom $z = -h(x)$. Surface displacement is given by the hydrostatic relation $g\eta = p|_{z=0}$. The upper-boundary condition is a linear free-surface $w|_{z=0} = \eta_t$, which can be applied at $z = 0$ provided $\eta << h$. The lower-boundary condition is an impermeable bottom $w|_{z=-h} = -h_x u|_{z=-h}$ (note that $-h_x$ indicates a positive bottom slope).

2.2.3   Depth-Averaging Over Topography

Decomposing surface and internal tides requires depth averaging variables and horizontal gradients of variables. To simplify notation, we introduce $\langle \cdot \rangle$ as the depth-average operator:

$$\langle \cdot \rangle = \frac{1}{h} \int_{-h}^{0} (\cdot) \mathrm{d}z' \ . \tag{2.6}$$

For consistency, all depth-averaged quantities will be denoted with uppercase letters and residuals by primes.

Over sloping topography, taking the depth average of a horizontal gradient requires the use of Leibniz's theorem (i.e., *Kundu and Cohen*, 2002)) and the product rule. The resulting identity is

$$\langle (\cdot)_x \rangle = \langle \cdot \rangle_x + \frac{h_x}{h} \left[\langle \cdot \rangle - (\cdot)|_{z=-h} \right] \ . \tag{2.7}$$

The first term on the right-hand side is the horizontal derivative of the depth-averaged quantity. If h does not depend on x, this is the only term on the right-hand side. The first part of the second term on the right-hand side is due to applying the product rule after integration, since the normalization factor $1/h$ depends on x. The last part of the second term on the right-hand side is due to the x-dependence in the bottom limit of integration.

2.2.4   Decomposing Horizontal Velocity

We use depth averaging to decompose horizontal surface- and internal-tide velocity as:

$$(U, V) = (\langle u \rangle, \langle v \rangle) \tag{2.8}$$

$$(u', v') = (u - U, v - V) \ , \tag{2.9}$$

respectively. Although the decomposition defined by (2.8) and (2.9) has not been formally justified over topography (to our knowledge), it is widely accepted/applied by the oceanographic community.

Approximating surface-tide velocity as a depth-average assumes that the surface tide produces all volume convergence and surface displacement. This property is illustrated by depth-integrating (2.4) using (2.7) to obtain

$$(HU)_x + \eta_t = 0 \ . \tag{2.10}$$

This approximation is consistent with both normal-modes over a flat bottom and the shallow-water equations commonly employed in surface-tide models containing complex topography (e.g., *Egbert and Ray*, 2000). A convenience of this decomposition is that surface-tide momentum balances can be obtained by depth-averaging (2.1) and (2.2).

For the internal tide, (2.10) is a rigid-lid boundary condition. Although smaller than surface tides, it is well known that internal tides produce surface displacements (e.g., *Ray and Mitchum*, 1996). Provided these displacements are small, they can be estimated from internal tide pressure at $z = 0$ using the hydrostatic relation (e.g., *Gill*, 1982). Requiring internal-tide velocity to have zero depth-average over topography is consistent with the modes derived by *Wunsch* (1969) for internal waves in a wedge-shaped domain.

2.2.5 Decomposing Pressure

The decomposition of pressure into surface and internal tide components has been debated for over a decade (*Holloway*, 1996; *Lu et al.*, 2001; *Kunze et al.*, 2002; *Gerkema and van Haren*, 2007) because it defines both internal-tide energy flux and surface-to-internal-tide

energy conversion. Here, we examine how an arbitrary decomposition influences the surface- and internal-tide momentum balances. Without loss of generality, we define surface- and internal-tide pressure as:

$$p^s(x, z) = P + \hat{p} \,, \tag{2.11}$$

$$p^i(x, z) = p' - \hat{p} \,, \tag{2.12}$$

respectively, where $\hat{p}(x, z)$ is an arbitrary pressure field, $P(x) = \langle p \rangle$ and $p'(x, z) = p - P$. The benefit of writing pressure using P, p', and $\hat{p}$ is that terms involving depth integrals are interpreted easily and role of $\hat{p}$ is isolated (which contains any depth dependence of the surface tide). Pressure terms and descriptions are listed in Table 2.1.

2.2.6   Decomposing the Equations of Motion

Surface- and internal-tide momentum equations illuminate the implications of choosing a pressure decomposition. The surface-tide x-momentum equation is formed by first depth-averaging (2.1) using (2.7), then both adding and subtracting $\hat{p}_x$. The surface-tide z-momentum and buoyancy equations are produced by kinematically decomposing (2.3) and (2.5):

$$U_t - fV = -p_x^s - (D - \hat{p}_x) \tag{2.13}$$

$$0 = -\hat{p}_z + \hat{b} \tag{2.14}$$

$$\hat{b}_t + N^2 \hat{w} = 0 \,, \tag{2.15}$$

where D is the internal-wave drag due to sloping topography:

$$D(x) = \frac{-h_x}{h} p'|_{z=-h} \ .$$ (2.16)

Internal-tide equations are obtained by differencing (2.13)-(2.15) with (2.1), (2.3), and (2.5), respectively:

$$u'_t - fv' = -p^i_x + (D - \hat{p}_x)$$ (2.17)

$$0 = -p^i_z + b^i$$ (2.18)

$$b^i_t + N^2 w^i = 0$$ (2.19)

where $b^i = b - \hat{b}$ and $w^i = w - \hat{w}$.

The surface- and internal-tide x-momentum equations are dynamically coupled through $D - \hat{p}_x$, which represents internal-wave drag and an arbitrary pressure gradient. Although it is expected that this term will convert momentum from the surface to internal tide, it is also possible for a shoaling internal tide to induce a surface tide. For instance, the internal-wave modes in a wedge-shaped domain derived by *Wunsch* (1969) have $U = 0$ but $P \neq 0$ and $D \neq 0$.

2.3 Choosing a Decomposition

It is possible to characterize several surface/internal-tide decompositions by their designation of $\hat{p}$. Here, we review four previously used decompositions and suggest a fifth (Section 2.3.4).

2.3.1 Using an Unstratified Fluid

Baines (1982) suggested that the surface tide could be determined from an unstratified flow. Such a decomposition requires $\hat{p} = p^B$ where:

$$p^B(x) = P_0 - P \tag{2.20}$$

and $P_0(x)$ is the pressure obtained from an identically forced but unstratified fluid. Although this decomposition has been employed in several studies (e.g., *Niwa and Hibiya*, 2001; *Khatiwala*, 2003; *Legg and Huijts*, 2006), it is physically problematic because it implies the surface tide is independent of the internal tide and internal-wave drag, which are determined by stratification. In practice, this decomposition requires that the surface tide not exchange energy with the internal tide. Although this might be a reasonable approximation for the surface tide, even a small error in surface-tide pressure $O(10^4 \text{ Pa})$ could result in a massive error in internal-tide pressure $O(10^2 \text{ Pa})$. In situations where the surface tide is boundary forced and/or freely propagating, it is subject to internal-wave drag and cannot be obtained accurately from an unstratified fluid.

2.3.2 Eliminating Wave Drag

Gerkema and van Haren (2007) assumed *a priori* that (2.13) and (2.17) are not coupled through internal-wave drag and implicitly required $\hat{p}_x = D$. This decomposition results in $\hat{p} = p^G$, where

$$p^G(x) = \int_{x_0}^x \frac{h_x}{h} p'|_{z=-h} \mathrm{d}x . \tag{2.21}$$

Gerkema and van Haren (2007) fail to recognize that their surface- and internal-tide momentum equations predetermine internal-tide pressure (and its constant of integration), leading them to incorrectly conclude that $\hat{p}$ cannot generally be zero over sloping topography. Equations (2.13) and (2.17) include coupling, and contradict their findings by indicating that $\hat{p}$ can equal zero.

p^G is problematic because it depends on a horizontal integral that is path-dependent. For instance, starting in a flat region and evaluating (2.21) along a path where $p'|_{z=-h} > 0$ up a slope to another flat region results in a net decrease in p^G. Such a decrease is unphysical because normal modes require $p^G = 0$ in both flat regions. Because of this inconsistency (which is further demonstrated in Section 2.4 using numerical simulations), this decomposition does not meet the requisites of Section 2.2.1.

2.3.3   Depth-Averaging

Kunze et al. (2002) defined internal-tide pressure as total pressure minus its depth-average, effectively setting $\hat{p} = 0$. Such a decomposition has been used to interpret the depth-structure of internal-tide energy flux (e.g., *Nash et al.*, 2005) and surface-to-internal-tide conversion in numerical simulations (e.g., *Kurapov et al.*, 2003). In order to examine the physical implications of this decomposition, it is useful to derive separate surface- and internal-tide energy balances. Depth-integrated energy equations are produced by dotting surface- and internal-tide momentum equations with total velocity and integrating (e.g., *Simmons et al.*, 2004; *Carter et al.*, 2008). The resulting equations are similar to those obtained by *Kurapov et al.* (2003) (with the omission of nonlinear terms and terms involving

the depth-structure of $\hat{w}$, which is zero here):

$$\frac{h}{2}\left(U^2 + V^2 + \frac{g\eta^2}{h}\right)_t = -\langle hUP\rangle_x - C_T - C_S \tag{2.22}$$

$$\frac{h}{2}\left\langle u'^2 + v'^2 + \frac{b^2}{N^2}\right\rangle_t = -\langle hu'p'\rangle_x + C_T + C_S \,. \tag{2.23}$$

The left-hand sides contain time-change in kinetic energy $(u^2 + v^2)/2$, and two forms of potential energy: $b^2/(2N^2)$ and $g\eta^2/2$. The right-hand sides contain energy-flux divergence and energy conversion. The equations are attractive because variables are simple to calculate, and potential energy and energy flux are naturally decomposed.

The first energy conversion term,

$$C_T(x) = -h_x U p'|_{z=-h} \tag{2.24}$$

represents topographic internal-tide generation and can be traced back to internal-wave drag in the momentum equations. C_T is a generic expression for work done on topography by tidal flow and has been used in numerous studies of internal tides (*Niwa and Hibiya*, 2001; *Llewellyn Smith and Young*, 2002; *Khatiwala*, 2003; *Gerkema et al.*, 2004; *Kurapov et al.*, 2003; *Legg and Huijts*, 2006; *Carter et al.*, 2008). It depends on the topographic gradient $-h_x$, surface tide velocity U, and internal-tide pressure at the bottom boundary $p'|_{z=h}$. Although $p'|_{z=0}$ can be extracted from numerical simulations and observations, linear theory has also been used to obtain analytical estimates of C_T (e.g., *Bell*, 1975b; *Khatiwala*, 2003; *Llewellyn Smith and Young*, 2002). These linear analytical estimates can be calculated over arbitrary topography following a procedure outlined by *Nycander* (2005), which *Zilberman et al.* (2009) found compared favorably with conversion estimates obtained using $p'|_{z=-h}$ from high-resolution numerical simulations.

The second energy conversion term,

$$C_S(x) = -\eta_t p'|_{z=0} \tag{2.25}$$

has been identified in several studies (*Craig*, 1987; *Kurapov et al.*, 2003; *Carter et al.*, 2008) and arises because the surface and internal tides do not individually satisfy the linear free-surface boundary condition. Specifically, surface- and internal-tide motions are dynamically coupled through (2.10), where $(hU)_x$ is a surface-tide term and $\eta_t = w^i|_{z=0}$ an internal-tide term. *Kurapov et al.* (2003) identified C_S as an error in the surface/internal-tide decomposition, pointing out that it is non-zero even over a flat bottom and contradicts the physics of normal modes. *Craig* (1987) also identified C_S but simply considered it an error in the internal-tide energy budget. The surface/internal-tide decomposition suggested by *Kunze et al.* (2002) thus provides a physically interpretable conversion term C_T but also contains an error represented by C_S.

2.3.4   Including Surface Motion

Here, we amend the surface/internal-tide decomposition presented in Section 2.3.3 to eliminate spurious energy conversion through the free-surface, C_S. Our choice of $\hat{p}$ is motivated from the energy equations for normal modes over a flat bottom, where C_S is canceled by a cross-term involving internal-tide velocity and surface-tide pressure (Appendix). Over arbitrary topography, this cross-term can be reproduced by requiring

$\hat{p} = p^\eta$ and defining:

$$w^\eta(x, z) = \eta_t \left(\frac{z + h}{h} \right) \tag{2.26}$$

$$b^\eta(x, z) = -N^2 \eta \left(\frac{z + h}{h} \right) \tag{2.27}$$

$$p^\eta(x, z) = \int_0^z b^\eta \mathrm{d}z' + c \,. \tag{2.28}$$

The constant $c(x)$ is determined by requiring $\langle p^\eta \rangle = 0$, assuring that, like the normal-mode solution, internal-tide pressure has zero depth-average. Sample time-series of p' and p^η (Fig. 2.1b-c) from a numerical simulation (see Section 2.4.3 for details) illustrates that p^η is surface intensified and has constant phase with depth. The magnitude of p^η is largest at high and low tides. Subtracting p^η from p' also changes the depth-profiles of instantaneous and tidally-averaged energy flux (Fig. 2.1f-g), the magnitudes of which depend on how u' is phased with p^η.

In order to remove C_S from the energy equations, it is also required that $(u'p^\eta)_x \approx u'_x p^\eta$. This relation arises from scaling the normal-mode energy equations and indicates that the surface tide has much longer wavelength than the internal tide. This approximation must be applied with caution over steep topography. However, the applicability of the linear free-surface is also at stake if the horizontal wavelength of the surface tide becomes too short. Setting $p^i = p' - p^\eta$, $p^s = P + p^\eta$, and $b^i = b - b^\eta$ results in the energy equations:

$$\frac{h}{2} \left\langle U^2 + V^2 + \frac{b^{\eta 2}}{N^2} + \frac{g\eta^{s2}}{h} \right\rangle_t = -\langle hUp^s \rangle_x - C_T \tag{2.29}$$

$$\frac{h}{2} \left\langle u'^2 + v'^2 + \frac{b^{i2}}{N^2} \right\rangle_t = -\langle hu'p^i \rangle_x + C_T \,, \tag{2.30}$$

where $g\eta^s = p^s|_{z=0}$ and C_T is given by (2.24). Equation (2.30) was also simplified using

$h \langle w^\eta b^i \rangle = \eta_t p^i|_{z=0}$, from integration by parts. This surface/internal-tide decomposition is ideal because it is consistent with normal modes and all energy conversion occurs through topographic internal-tide generation, C_T.

2.3.5   Including Topographic Heaving

Lu et al. (2001) effectively set $\hat{p} = p^\eta + p^h$, which includes both pressure due to isopycnal heaving by movement of the free surface p^η, and pressure due to isopycnal heaving by the surface tide at sloping topography p^h. The effect of topographic heaving is described by:

$$w^h(x, z) = h_x U \frac{z}{h} \tag{2.31}$$

$$b^h(x, z) = \frac{N^2}{i\omega} h_x U \frac{z}{h} \tag{2.32}$$

$$p^h(x, z) = \int_0^z b^h \, \mathrm{d}z' + c , \tag{2.33}$$

where $c(x)$ is determined by the requirement $\langle p^h \rangle = 0$. Although *Lu et al.* (2001) chose their decomposition primarily because it removed spurious energy conversion over a flat bottom (i.e. C_S), they asserted that topographic heaving is part of the "external mode of response" and should be included in the surface tide.

The energy budgets are slightly more complicated than those in Section 2.3.4, because the p_x^h is large over steep topography and it cannot be assumed that $\left(u' p^h \right)_x \approx u'_x p^h$. The resulting surface- and internal-tide energy equations are identical to (2.29) and (2.30) on the left-hand sides, but, contain different expressions for energy flux and energy conversion

on the right-hand side. The right-hand sides are now written:

$$= - \left\langle h \left(up - u'p^i \right) \right\rangle_x - C_T - C_F \tag{2.34}$$

$$= - \left\langle hu'p^i \right\rangle_x + C_T + C_F \tag{2.35}$$

where $p^i = p' - \left(p^\eta + p^h \right)$, C_T is given by (2.24), and C_F is a new surface-to-internal-tide energy conversion term:

$$C_F(x) = - \left\langle hu'p^h \right\rangle_x . \tag{2.36}$$

A complication in (2.34) is that surface-tide energy flux is defined as the total minus the internal-tide component. Such a division is more *ad hoc* than physically intuitive. C_F is suspicious because the divergence theorem requires that it integrate to zero over isolated topographic features. Therefore, C_F changes the distribution of topographic internal-tide generation but has no net contribution. In the next section, we find that including p^h in surface-tide pressure results in unphysical distributions of energy flux and internal-tide generation for three numerical simulations.

2.4   Assessing the Decompositions

In the following, we assess the merits of each decomposition presented in Section 2.3 by evaluating them using numerical simulations and observations of tidal flow over topography.

2.4.1 Tidally-Averaged Energy Equations

Most time-dependence in the internal-tide energy equations is periodic. When forcing is constant, tidally-averaging (2.30), (2.23), and (2.35) produces:

$$\overline{\langle hu'(p' - p^\eta)\rangle}_x = \overline{C_T} \tag{2.37}$$

$$\overline{\langle hu'p'\rangle}_x = \overline{C_T} + \overline{C_S} \tag{2.38}$$

$$\overline{\langle hu'(p' - p^\eta - p^h)\rangle}_x = \overline{C_T} + \overline{C_F} , \tag{2.39}$$

respectively, where $\overline{(\cdot)}$ represents a time-average. These equations can be assessed using observed full-depth timeseries or numerical simulations.

2.4.2 Calculating p', p^B, p^G, p^η, and p^h

Although total pressure is calculated explicitly in models, it cannot be obtained from observations because

$$p(x, z) = \int_0^z b \ \mathrm{d}z' + c \tag{2.40}$$

has an undetermined constant of integration $c(x)$ which depends on surface displacement. However, determining p' from full-depth profiles of b is unambiguous even without measuring the absolute surface displacement. Starting with the measured quantity

$$p_m(x, z) = \int_0^z b \ \mathrm{d}z' , \tag{2.41}$$

the practical expressions for pressure are

$$\left(p, P, p'\right) = \left(p_m + c,\ \langle p_m \rangle + c,\ p_m - \langle p_m \rangle\right)\ . \tag{2.42}$$

so that p' does not depend on the unknown constant of integration.

But, the internal tide may also depend on a depth-dependent profile of pressure $\hat{p}(x, z)$, which can be more difficult to compute. For instance, p^B is calculated for our numerical simulations by conducting an identical but unstratified simulation. In the analysis of observations, p^B would be impossible to determine accurately. Additionally, calculating p^G is ambiguous in both observations and numerical simulations because the starting point and path of the integral are undetermined. In our analysis, we examine integrals originating from the left- and right-hand-sides of the domain, denoted p^{Gl} and p^{Gr}, respectively. Calculating p^η requires an estimate of η. Models calculate this term explicitly. In observations, it could be extracted from either the measured bottom pressure or estimated from a surface-tide model such as TPXO (*Egbert and Ray*, 2000). Finally, although, p^h appears straightforward to compute in both numerical simulations and observations, the appropriate horizontal scale for evaluating h_x is unclear. Our pragmatic approach for numerical simulations is to evaluate p^h at the finest resolution available.

2.4.3   Numerical Simulations

Simulations were performed using the MIT general circulation model (MITgcm), a nonlinear, non-hydrostatic, z-coordinate, implicit free-surface, finite-volume model (*Marshall et al.*, 1997). For simplicity, the domains are uniform in one horizontal direction (i.e. 2-D) but contain f-plane rotation. Horizontal resolution is 250 m near sloping

topography and smoothly transitions to 1000 m near the boundaries. Realistic stratification from the Oregon slope is used with a uniform vertical resolution of 20 m. Eddy viscosities of 5×10^{-1} m^2 s^{-1} in the horizontal and 5×10^{-2} m^2 s^{-1} in the vertical were employed for stability.

The first two simulations contain idealized sub- and super-critical continental slopes. The slopes are prescribed so that $s/a = 0.75$ and 1.25, respectively, where s is the topographic slope and $a = \sqrt{(\omega^2 - f^2)/(N^2 - \omega^2)}$ the slope of an M$_2$ internal-tide characteristic. The third simulation contains realistic topography from the site of an observational study of internal tides on the Oregon slope (*Nash et al.*, 2007; *Martini et al.*, 2011a). To minimize the effects of numerical lateral boundaries, the full model domains extend 400 km from the region of topographic interest.

Although realistic values are used in the simulations, two-dimensional domains make realistic forcing impossible. Simplified forcing is accomplished by prescribing a 0.05, 0.05, and 0.025 m s^{-1} semidiurnal depth-constant velocity along the open boundary for the sub-critical, super-critical, and Oregon topographies, respectively. The amplitudes of free-surface oscillations are 1.8, 1.8, and a realistic 0.9 m for the sub-critical, super-critical, and Oregon topographies, respectively. Two-thousand time-steps are used per tidal period. A flow-relaxation scheme applied at the boundaries prevents reflection of internal waves. All modeled quantities are averaged over the tenth tidal cycle when the energy balance has reached a nearly steady-state.

2.4.4   The Depth Structure of Energy Flux

The depth-structure of internal-tide energy flux, $\overline{u'p^i}$, is useful for interpreting numerical simulations and observations (e.g., *Kunze et al.*, 2002; *Althaus et al.*, 2003; *Nash et al.*,

2004, 2005, 2006; *Carter et al.*, 2006; *Gerkema and van Haren*, 2007; *Duda and Rainville*, 2008). The profiles defined by Sections 2.3.4 and 2.3.3, $\overline{u'(p'-p^\eta)}$ and $\overline{u'p'}$, are physically intuitive (Fig. 2.2, rows one and two) because they indicate that all internal-tide energy is propagating away from steep topography, the expected region of internal-tide generation. As suggested by theory (*Craig*, 1987), these profiles also represent beam-like energy flux to deep water. The beams reflect off the bottom near the base of the slope and off the surface near -75 km.

The other four representations of internal-tide energy flux produce distributions that are unphysical and confusing. For instance, the energy flux where topographic heaving has been removed from the internal tide, $\overline{u'(p'-p^\eta-p^h)}$, contains a discontinuity in energy flux along a vertical line extending upward from the base of the slope (Fig. 2.2, row three). There are also patches of onshore energy flux observed in the upper water column over the slope (0 to 25-50 km) that do not originate from a known source of the internal tide. Similarly unexplained energy-fluxes are obtained when an unstratified simulation is used to determine the surface tide, $\overline{u'(p'-p^B)}$ (Fig. 2.2, row four) (*Baines*, 1982). In particular, this surface/internal-tide decomposition indicates internal-tide energy propagating from regions where the bottom is flat and so there should be no internal-tide generation. The energy fluxes obtained by decomposing pressure to cancel out internal-wave drag, $\overline{u'(p'-p^{Gl})}$ and $\overline{u'(p'-p^{Gr})}$ (Fig. 2.2 rows five and six) have similar unphysical energy flux directed towards the expected generation region. Additionally, the renditions of this decomposition that integrate (2.21) from the left-hand and right-hand sides of the domain are drastically different, indicating sensitivity to the integral starting-point. In both cases, near the start of the integral, the energy flux is similar to that of $\overline{u'p'}$ but, as p^G is integrated over steep topography, the flux becomes unphysical, again indicating that internal-tide energy is originating over a flat bottom.

Because $p^i = p' - p^\eta$ is identified in Section 2.3.4 as the most physically relevant pressure decomposition, deviations from the resulting energy flux are quantified for each simulation. Percentages were calculated of root-mean-square difference in energy flux, normalized by the root-mean-square of $\overline{u'(p' - p^\eta)}$ averaged over the domain shown. These deviations, reported in Fig. 2.2, indicates that $\overline{u'p'}$ is the most similar to $\overline{u'(p' - p^\eta)}$, especially over steep topography. We also note that these two fluxes converge as surface displacement decreases and $p^\eta \to 0$. Other distributions of internal-tide energy flux have larger deviations from $\overline{u'(p' - p^\eta)}$, which range from 42% to 197%, and do not necessarily converge as $\eta \to 0$.

2.4.5   Conversion and Energy-Flux Divergence

Internal-tide generation and energy-flux divergence are important quantities for understanding internal-tide energetics. Although many studies equate these quantities, they may be substantially different due to energy dissipation (*Carter et al.*, 2008). The expressions for energy-flux divergence and energy conversion (2.37)-(2.39) are compared in Fig. 2.3 for each topography.

Although the spatial structure of surface-to-internal-tide conversion is different for each decomposition, it is always balanced by energy-flux divergence (to first order), indicating that the balances are self-consistent. Errors in the energy balance are attributed to time variability in internal-tide energy, energy advection and dissipation. Distributions of energy conversion when $p^i = p' - p^\eta$ and $p^i = p'$ (Fig. 2.3, rows two and three) are similar over topography, indicating internal-tide generation all along the slope. Conversely, when $p^i = p' - (p^\eta + p^h)$ (Fig. 2.3, row four), conversion is concentrated at the base of the slope as found by *Lu et al.* (2001). Because internal-tide generation is expected in regions of large $h_x N^2$ (*Baines*, 1982), which is constant in the sub- and super-critical simulations,

decompositions which result in conversion all along the slope are more physically intuitive than the decompositions where conversion is isolated at the base of the slope.

Over a flat bottom, normal modes require the surface and internal tides be dynamically uncoupled (Appendix). *Craig* (1987), *Lu et al.* (2001), and *Kurapov et al.* (2003) all identified energy conversion through the free surface in their energy budgets and attributed it to an error in the surface/internal-tide decomposition. This error causes spurious oscillations in energy flux that coincide with surface and bottom reflections of the internal tide. Removal of these oscillations may be important for quantifying non-linear effects associated with internal-tide reflection (*Althaus et al.*, 2003; *Gerkema et al.*, 2006). Here, the amplitude of spurious energy flux oscillations is 10-60% that of the total flux due to topographic internal-tide generation (Fig. 2.3, row one). An important consequence of defining internal-tide pressure as $p^i = p' - p^\eta$ is the elimination of spurious energy conversion and the isolation of topographic internal-tide generation.

2.4.6   The role of p^η

In the sub-critical topography simulation (Fig. 2.3, row one), removing p^η from p' corrects internal-tide pressure at the peak ($x = -74$ km) and trough ($x = -126$ km) of an energy-flux oscillation. In both of these locations (Fig. 2.4), p^η is surface-intensified. For example, at low tide, p^η dominates $p^i = p' - p^\eta$ at $x = -74$ km (because $p' \ll p^\eta$), and it represents half of p^i at $x = -126$ km. Correcting internal-tide pressure increases time-averaged offshore energy-flux at $x = -74$ km and halves offshore energy flux at $x = -126$ km (Fig. 2.4a). This result indicates that computation of energy flux without accounting for p^η (i.e., following *Kunze et al.*, 2002) produces unphysical energy-flux divergences and convergences that have the potential for being misinterpreted as nonlinear processes and/or turbulent dissipation.

2.4.7 Consequences for the Analysis of Observations

Here, we examine the effect of p^η in two observational studies of internal-tides. Energy fluxes were corrected by using $p^i = p' - p^\eta$ rather than $p^i = p'$ at four stations at Kaena Ridge, Hawaii (*Nash et al.*, 2006) and five stations at the Oregon continental slope (*Nash et al.*, 2007; *Martini et al.*, 2011a) (Table 2.2). Surface displacements estimated from TPXO are six times smaller at Kaena Ridge (0.14 m) than the Oregon slope (0.92 m) but the tidally-averaged depth-integrated internal-tide energy flux at Kaena Ridge O(10 kW m^{-1}) is much larger that that on the Oregon slope O(500 W m^{-1}). In both locations, energy flux corrections (defined as $-\langle \overline{hu'p^\eta} \rangle$) are 10-50 W m^{-1}. At Kaena Ridge, large depth-variability in p' marginalizes the role of p^η in both the depth-profile of internal-tide pressure and energy flux (Fig. 2.5a-d). On the Oregon slope, p^η has a noticeable impact on the depth-profile of internal-tide pressure and energy flux, particularly at the surface (Fig. 2.5e-h).

2.5 Conclusions

Five surface/internal-tide decompositions have been expressed using different divisions of pressure. The most satisfactory decomposition results from defining internal-tide pressure as $p^i = p' - p^\eta$, where p^η is due to isopycnal heaving by movement of the free-surface. However, other decompositions also provide insight into the physics of topographic internal-tide generation. Inconsistencies arising when the surface tide is obtained from an unstratified flow (*Baines*, 1982) reveal the important effects of internal-wave drag on the surface tide. Small perturbations from the surface tide create significant changes in the depth-structure of internal-tide energy flux, making it impossible to interpret physically. Similarly, when pressure is decomposed to eliminate internal-wave drag (*Gerkema and van Haren*, 2007), the

resulting depth-structure of internal-tide energy fluxes are both sensitive to an undetermined limit of integration, and indicate energy propagating from regions where there is no internal-tide generation.

Using a simple depth-average to decompose pressure results in spurious surface-to-internal-tide energy conversion over a flat bottom. Closely examining the energetics of normal modes (Appendix) motivates the inclusion of a pressure profile p^η in the surface tide which accounts for movement of the free surface, even over a sloping bottom. The careful elimination of energy conversion related to the free surface confirms the interpretation that C_S is an error in the surface/internal-tide decomposition and does not have physical relevance.

Including pressure due to topographic heaving p^h in the surface tide results in spatial distributions of internal-tide energy flux and topographic internal-tide generation that are inconsistent with theory. This finding indicates that all topographic heaving is a component of the internal tide, not the surface tide.

Derivation and assessment of these surface/internal-tide decompositions also leads to several practical conclusions:

1) The most satisfactory surface/internal-tide decomposition is described in Section 2.3.4 and defines internal tide pressure as $p^i = p' - p^\eta$ (2.28). The inclusion of p^η is crucial for eliminating spurious surface-to-internal-tide energy conversion, C_S. In other words, convergences in $u'p'$ computed following *Kunze et al.* (2002) are not entirely associated with turbulent dissipation, but also have a contribution from p^η through $-\langle \overline{hu'p^\eta} \rangle$.

2) In the tidally-averaged internal-tidal energy equation (2.37), depth-integrated internal-tide energy-flux divergence is balanced by topographic internal-tide generation $C_T = -h_x U p'|_{z=-h}$, which arises from internal-wave drag.

3) The depth-structure of internal-tide energy flux, $u'(p' - p^\eta)$, is unambiguous and can

be computed as long as an estimate of surface displacement and full-depth timeseries of velocity and buoyancy are available. When surface displacements are small $p^\eta \approx 0$ and internal-tide energy flux is equivalent to $u'p'$ as proposed by *Kunze et al.* (2002).

4) Observations over Kaena Ridge, Hawaii and the Oregon continental slope indicate p^η alters depth-integrated internal-tide energy flux by 10-50 W m^{-1}. Changes in the depth-structure of energy flux due to p^η are unimportant over Kaena Ridge, but non-negligible near the surface over the Oregon slope. Over continental shelves, where internal-tide energy-flux and topographic generation are reduced, p^η can have increased importance (*Kurapov et al.*, 2003).

Separating the surface and internal tides correctly over steep topography is challenging. Although the decomposition suggested here will likely be improved by future investigations, it currently provides a complete, consistent, and practical method for examining internal-tide energetics.

2.6   Appendix: Modes Over a Flat Bottom

Normal modes over a flat bottom provide a physical description of surface and internal tides as dynamically-uncoupled waves (e.g., *Wunsch*, 1975; *Gill*, 1982; *Pedlosky*, 2003). Here we review the formulation of the problem, approximate the solutions, and scale the modal-energy equations.

All variables are represented as a series of modes using separation of variables:

$$(u, v, p) = \sum_{n=0}^{\infty} (\hat{u}_n, \, \hat{v}_n, \, \hat{p}_n) \, F_{n,z} \tag{2.43}$$

$$(w, b) = \sum_{n=0}^{\infty} \left(\hat{w}_n, \, \hat{b}_n \right) F_n \tag{2.44}$$

where hats denote the modal amplitude, which contains the x-dependence, and $F_{n,z}(z)$ is the z-derivative of the nth vertical-structure function. Each mode satisfies the following differential equations in frequency space [i.e. $(\cdot)_t = -i\omega(\cdot)$]:

$$F_{n,zz} + \frac{1}{c_n^2} N^2 F_n = 0 \tag{2.45}$$

$$\hat{w}_n + \frac{1}{c_n^2} i\omega \, \hat{p}_n = 0 \tag{2.46}$$

where c_n are modal phase-speeds and $1/c_n$ eigenvalues. The boundary conditions are a linear free-surface: $F_{n,z} = g/c_n^2 F$ at $z = 0$ and flat bottom: $F_n = 0$ at $z = -h$. This derivation assumes constant stratification, but can be extended to situations of slowly varying $N^2(z)$ by applying WKBJ normalization (*Munk*, 1981). One set of solutions to (2.45)-(2.46) is:

$$F_n = \frac{c_n}{N} \, \sin\left[\frac{N}{c_n} (z + h)\right] \tag{2.47}$$

where c_n must be determined by the surface boundary condition:

$$\tan\left[\frac{N\,h}{c_n}\right] = \left(\frac{N^2 h}{g}\right) \frac{c_n}{N\,h} \, , \tag{2.48}$$

and the non-dimensional parameter $\epsilon = N^2 h/g$ is normally much less than 1% in the deep ocean (e.g., *Pedlosky*, 2003). Although c_n may be solved numerically in (2.48), they may also be approximated analytically when $c_n/(Nh)$ is very small or large. When $c_n/(Nh)$ is $O(1)$, the right-hand side of (2.48) is nearly zero and $c_n = Nh/(n\pi)$ where $n \geq 1$. These modes represent the internal tide and are consistent with a rigid-lid boundary condition. However, if $n = 0$, then $c_n/(Nh) >> 1$, and we should employ the small-angle approximation in (2.48) to obtain $c_0 = \sqrt{gh}$. The 0th mode describes the surface tide and

is not consistent with a rigid-lid boundary condition because it does not have infinite phase speed.

Using the approximated modal phase-speeds and the non-dimensional parameter, ϵ, the surface- and internal-tides are expanded in terms of $\hat{p}_n$. Because the vertical wavelength of the surface tide is much greater than h, the cosines and sines of this mode are expanded using a Taylor series to $O(\epsilon)$. The surface-tide solution is approximated:

$$p_0 = \hat{p}_0 \left[1 - \epsilon \frac{1}{2} \left(\frac{z+h}{h} \right)^2 \right] \tag{2.49}$$

$$b_0 = -\epsilon \frac{\hat{p}_0}{h} \left(\frac{z+h}{h} \right) \tag{2.50}$$

$$u_0 = \frac{\hat{p}_0}{c_0} \left(1 - \frac{\omega^2}{f^2} \right)^{-1} \left[1 - \epsilon \frac{1}{2} \left(\frac{z+h}{h} \right)^2 \right] \tag{2.51}$$

$$v_0 = -\frac{i\hat{p}_0 f}{c_0 \omega} \left(1 - \frac{\omega^2}{f^2} \right)^{-1} \left[1 - \epsilon \frac{1}{2} \left(\frac{z+h}{h} \right)^2 \right] \tag{2.52}$$

$$w_0 = -\frac{i\hat{p}_0 \omega h}{c_0^2} \left(\frac{z+h}{h} \right) \tag{2.53}$$

and the internal-tide solution:

$$p_n = \hat{p}_n \cos \left[\frac{n\pi}{h} (z+h) \right] \tag{2.54}$$

$$b_n = -\frac{\hat{p}_n n\pi}{h} \sin \left[\frac{n\pi}{h} (z+h) \right] \tag{2.55}$$

$$u_n = \frac{1}{\sqrt{\epsilon}} \frac{\hat{p}_n n\pi}{c_0} \left(1 - \frac{\omega^2}{f^2} \right)^{-1} \cos \left[\frac{n\pi}{h} (z+h) \right] \tag{2.56}$$

$$v_n = -\frac{1}{\sqrt{\epsilon}} \frac{i\hat{p}_n f n\pi}{c_0 \omega} \left(1 - \frac{\omega^2}{f^2} \right)^{-1} \cos \left[\frac{n\pi}{h} (z+h) \right] \tag{2.57}$$

$$w_n = -\frac{1}{\epsilon} \frac{i\hat{p}_n \omega h n\pi}{c_0^2} \sin \left[\frac{n\pi}{h} (z+h) \right] , \tag{2.58}$$

where and (2.54)-(2.58) can be summed over all n to account for the complete internal tide.

Next, modal-energy equations are formed by depth-integrating the dot product of the nth mode and total velocity. Horizontal derivatives can be written $(\cdot)_x = i\omega/c_n$ (which is proportional $1/\sqrt{\epsilon}$ for $n > 0$). Using (2.49)-(2.58) the first-order surface and internal tide energy balances are:

$$\frac{h}{2}\left\langle u_0^2 + v_0^2 + \frac{g\eta_0^2}{h} \right\rangle_t = -\langle hu_0p_0\rangle_x - h\langle u_np_0\rangle_x \tag{2.59}$$

$$+ h\langle w_nb_0\rangle + O(\sqrt{\epsilon})$$

$$\frac{h}{2}\left\langle u_n^2 + v_n^2 + \frac{b_n^2}{N^2} \right\rangle_t = -\langle hu_np_n\rangle_x - \eta_tp_n|_{z=0} \tag{2.60}$$

$$+ h\langle w_nb_0\rangle + O(\sqrt{\epsilon}) \,,$$

respectively, where the relation $\langle w_nb_0\rangle = \langle w_0b_n\rangle$ has been used.

These equations have several interesting properties. First, the surface tide contains all the free-surface energy but has no internal energy (i.e. $\langle b_0^2/N^2\rangle \propto \epsilon$). Furthermore, free-surface energy is only determined by the surface-tide pressure at $z = 0$ (i.e. η_0 not simply η), consistent with the internal tide obeying a rigid lid. Secondly, it is nonintuitive that curvature is important in the depth-structure of p_0 but not u_0. For instance, $\langle u_np_0\rangle_x \propto 1$ while $\langle u_0p_n\rangle_x \propto \sqrt{\epsilon}$. These scalings are a result of p_0 being a factor of c_0 larger than u_0, while p_n is only a factor of $c_0\sqrt{\epsilon}/(n\pi)$ larger than u_n. Lastly, it is interesting that two modal cross-terms are present in each equation. These represent energy conversion, however, the modes are dynamically independent because the terms cancel each other. Summing over all n, and using the notation of Section 2.3.4, these relations can be written:

$$\eta_tp^i|_{z=0} = h\left\langle u'p^\eta \right\rangle_x = h\left\langle w^ib^\eta \right\rangle \,, \tag{2.61}$$

where $C_S = -\eta_t p'|_{z=0}$ has been previously interpreted as spurious surface-to-internal-tide energy conversion.

Acknowledgments
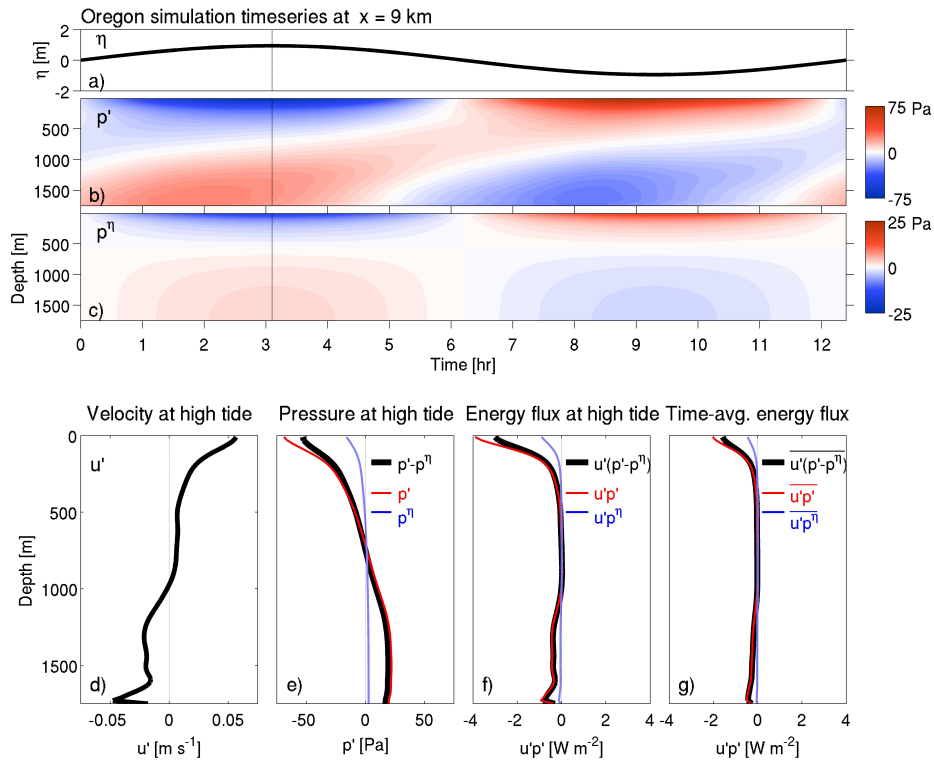
Figure 2.1: a) Timeseries of η from Oregon topography simulation, vertical line indicates high tide. (b) Timeseries of p'. (c) Timeseries of p^η. (d) u' at high tide. (e) $p' - p^\eta$ (black), p' (red), and p^η (blue) at low tide. (f) Energy flux at high tide. (g) Energy flux averaged over a tidal period.
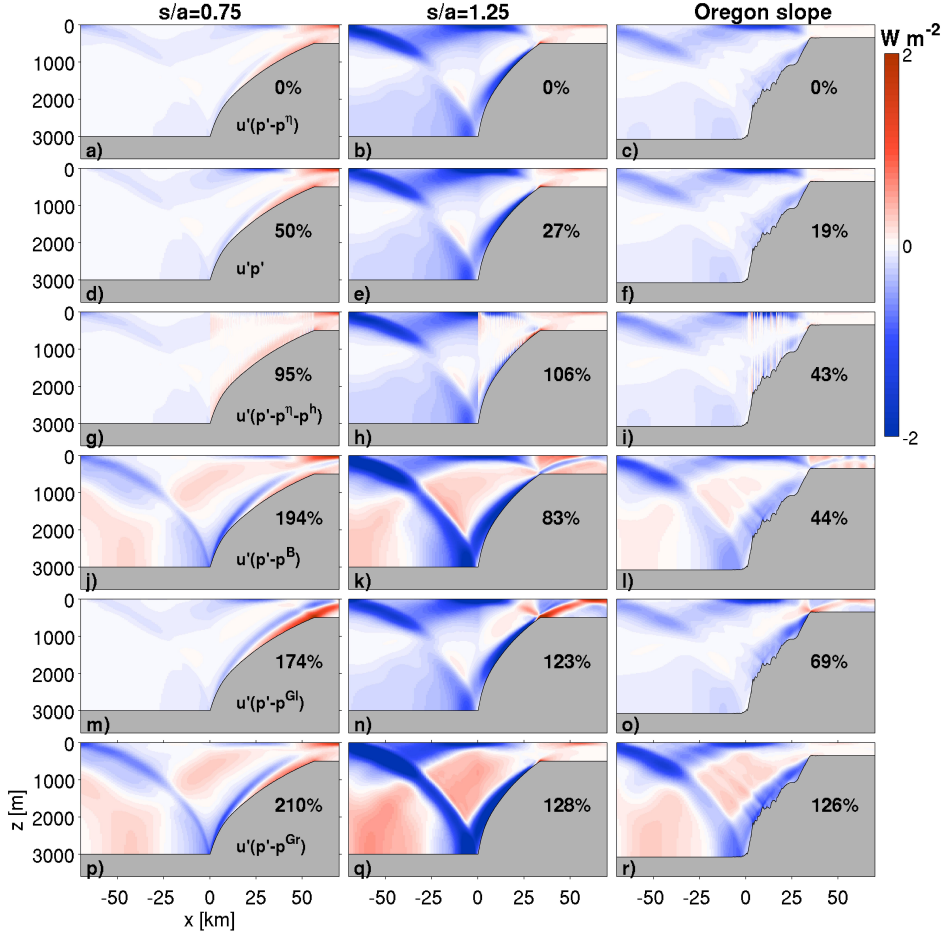
Figure 2.2: Depth-structure of tidally-averaged internal-tide energy flux for sub-critical, super-critical, and Oregon slope topographies. Row one: spatial structure of $\overline{u'(p'-p^\eta)}$. Rows two through six: spatial structure of $\overline{u'p'}$, $\overline{u'(p'-p^\eta-p^h)}$, $\overline{u'(p'-p^B)}$, $\overline{u'(p'-p^{Gl})}$, and $\overline{u'(p'-p^{Gr})}$, respectively. p^{Gl} and p^{Gr} are integrated from the left- and right-hand-sides of the domain, respectively. Percentages indicate average root-mean-square difference between the plotted energy flux and $\overline{u'(p'-p^\eta)}$, normalized by the root-mean-square of $\overline{u'(p'-p^\eta)}$.
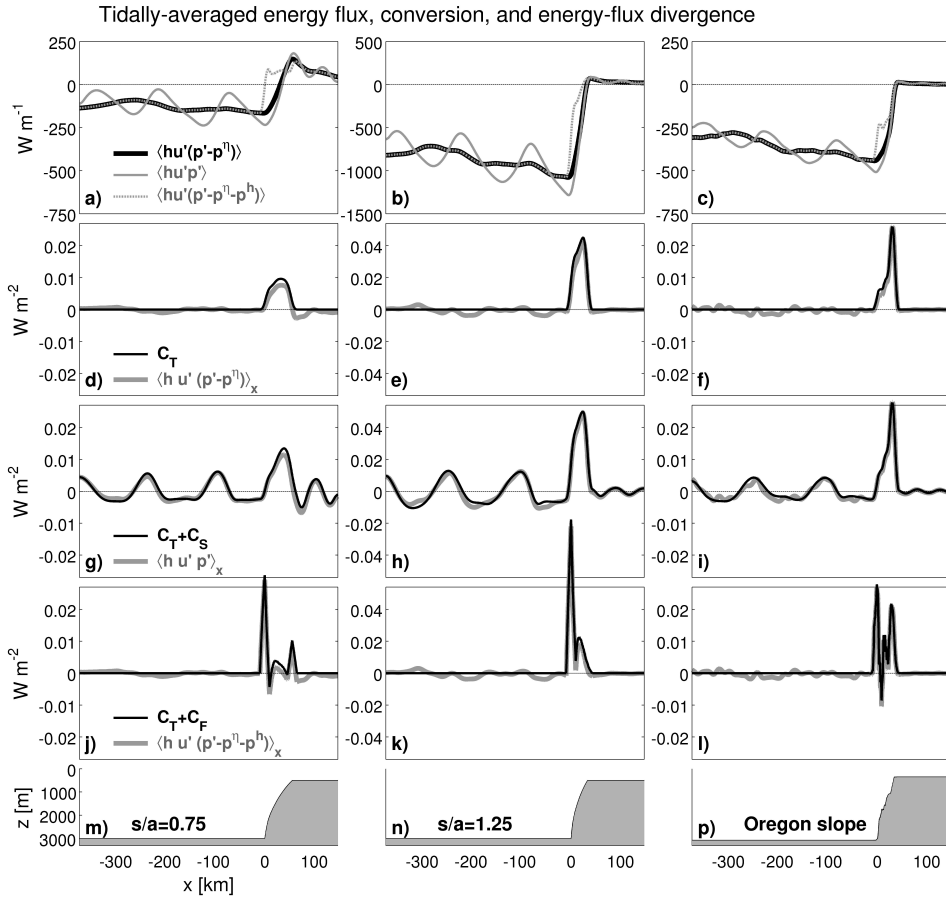
Figure 2.3: First row: Tidally-averaged depth-integrated energy fluxes. Second through fourth rows: Energy-flux divergence (gray) and conversion (black), see (2.37)-(2.39), respectively. All trends are smoothed by a double running average with span of 10 km. Bottom row: Sub-critical, super-critical, and Oregon slope topographies.
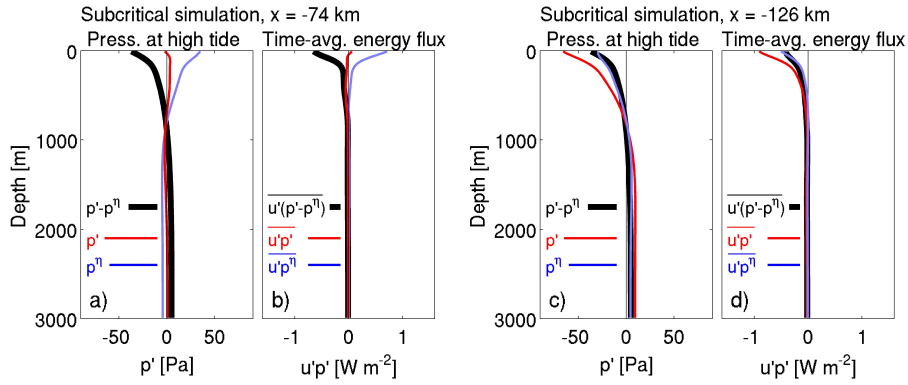
Figure 2.4: Effect of p^η at two locations in the sub-critical simulation. (a) At low tide, $-p^\eta$ dominates $p' - p^\eta$. (b) Time-averaged energy flux is dominated by $-\langle \overline{u'p^\eta} \rangle$. (c) At low tide, p^η represents half of the magnitude of p^i. (d) Subtracting $\langle \overline{u'p^\eta} \rangle$ reduces the time-averaged energy flux by half.
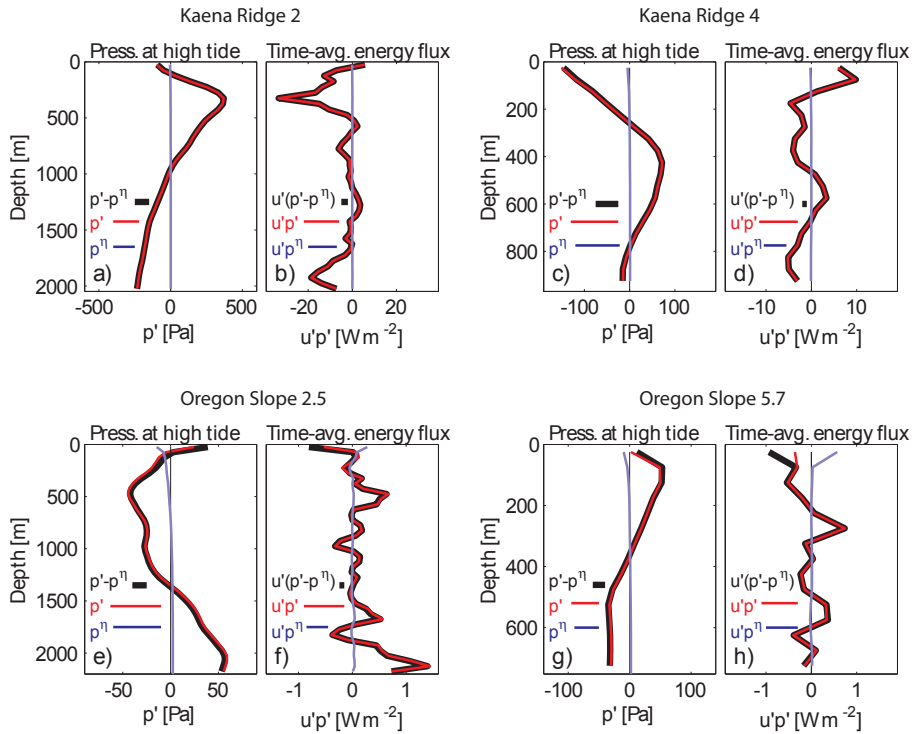
Figure 2.5: Effect of p^η in observations. Kaena Ridge, deep location: (a) $p' - p^\eta$ (black) is indiscernible from p' (red) at low tide. (b) Time-averaged energy fluxes are indiscernible. Kaena Ridge, shallow location: pressures (c) and energy fluxes (d) are indiscernible. Oregon slope, deep location: (e) p^η impacts $p' - p^\eta$ near the surface at low tide. (f) Offshore energy flux is enhanced by subtracting $\langle \overline{u'p^\eta} \rangle$ in the upper 100 m. Oregon slope, shallow location: (g) p^η is largest near the surface at low tide. (h) Subtracting $\langle \overline{u'p^\eta} \rangle$ nearly doubles the offshore energy flux in the upper 100 m.

Table 2.1: Summary of pressure terms

Term	Description
$p(x,z)$	Total
$P(x)$	Depth-average
$p'(x,z) = p - P$	Residual
$p^s(x,z) = P + \hat{p}$	Surface tide
$p^i(x,z) = p' - \hat{p}$	Internal tide
$\hat{p}(x,z)$	Arbitrary profile
$P_0(x)$	Identical but unstratified fluid
$p^B(x)$	Unstratified minus depth-average
$p^G(x)$	Balances wave-drag
$p^\eta(x,z)$	Due to free-surface isopycnal-heaving
$p^h(x,z)$	Due to topographic isopycnal-heaving

Table 2.2: Summary of re-analysed observations of energy flux at selected sites from Kaena Ridge [KR; *Nash et al. 2006*] and the Oregon Slope [OR; *Nash et al. 2007*]. Energy Flux was computed as $\langle \overline{u'(p'-p^\eta)} \rangle$. The correction represents $-\langle \overline{u'p^\eta} \rangle$.

Site	Depth [m]	η [m]	Energy Flux [W m^{-1}]	Correction [W m^{-1}]
KR 2	2048	0.14	-10294	-7
KR 3	1300	0.14	-4086	+10
KR 4	969	0.14	-63	+43
KR 5	970	0.14	-3058	+50
OR 2.5	2204	0.92	332	-35
OR 3.3	1714	0.91	535	-57
OR 4.3	1241	0.92	123	-31
OR 5.3	1025	0.92	54	-13
OR 5.7	752	0.92	-75	-33

3. A DIRECT COMPARISON OF INTERNAL-TIDE PRESSURES

3.1 Introduction

The decomposition of surface and internal tides determines important properties such as the surface and internal-tide momentum equations and the vertical structure of internal-tide energy flux (*Kelly et al.*, 2010, hereafter KNK10). A standard decomposition of velocity defines surface-tide velocity as the depth average, $U = \langle u \rangle$, and internal-tide velocity as the residual, $u' = u - U$. However, there remains debate over the best decomposition of pressure (T. Gerkema, personal correspondence). Particularly, for *Wunsch* (1968)'s solution to waves in a wedge-shaped domain. The decomposition of *Kunze et al.* (2002) suggests that pressure can be decomposed analogously to velocity, defining $p' = p - \langle p \rangle$ as internal-tide pressure and, by default, $P = \langle p \rangle$ as surface tide pressure. This decomposition is supported by KNK10 (here we assume a rigid lid so that p^η, KNK10's correction to *Kunze et al.* (2002), is zero.) However, *Gerkema and van Haren* (2007) (hereafter GvH07) challenge this notion, asserting that internal-tide pressure does not have zero depth-average over sloping topography.

KNK10 noted that surface and internal-tide momentum equations are determined by the decomposition of pressure. In Section 3.2, we reexamine the internal-tide momentum equations of KNK10 and GvH07. In Section 3.3, we discuss methods for assessing the internal-tide pressures supported by KNK10 and GvH07. In Section 3.4, we examine the internal-tide pressures for waves in a wedge-shaped domain (*Wunsch*, 1968, 1969) and examine their compatibility with the normal-mode description of internal tides over a flat bottom. In Section 3.5, it is concluded that internal-tide pressure is defined by p' (*Kunze*

et al., 2002, KNK10) because it is compatible with the normal-mode description of internal tides over a flat bottom and produces an unambiguous description of tidal dynamics.

3.2   Internal-Tide Momentum Equations

The non-rotating, linear, horizontal momentum equation is

$$u_t = -p_x \tag{3.1}$$

where subscripts indicate partial derivatives. For the present study, we consider a rigid lid at $z = 0$ and a sloping bottom at $z = -h(x)$. Applying the standard decomposition of velocity, depth-averaging (3.1) and calculating its residual produces the surface and internal-tide momentum equations

$$U_t = -P_x + \frac{h_x}{h} p'|_{z=-h} \tag{3.2}$$

$$u'_t = -p'_x - \frac{h_x}{h} p'|_{z=-h} , \tag{3.3}$$

respectively (KNK10). We note that, regardless of the physical interpretation of P and p', the mathematical expressions on the right-hand sides of (3.2) and (3.3) always balance surface and internal-tide accelerations, respectively.

KNK10 interpreted the coupling term in (3.2) and (3.3) as internal-wave drag and showed that it resulted in topographic internal-tide generation in the depth-integrated internal-tide energy equations.

GvH07 proposed a different internal-tide momentum equation, simply assuming that

(3.1) applied to internal-tide fields

$$u'_t = -p^i_x \, , \qquad (3.4)$$

where p^i is their definition of internal-tide pressure and there is no coupling through internal-wave drag. Comparing (3.3) with (3.4), it is evident that this assumption produces $p^i \neq p'$. Without justifying their internal-tide momentum equation, GvH07 used this result to discredit *Kunze et al.* (2002) and the numerous papers that have utilized their decomposition.

GvH07's definition of internal-tide pressure is obtained by equating (3.3) with (3.4) and horizontally integrating

$$p^i = p' + \int_{x_0}^{x} \frac{h_x}{h} p'|_{z=-h} \mathrm{d}x' \, , \qquad (3.5)$$

which depends on an integral with undetermined limit x_0. For special cases with $U = 0$, such as waves in a wedge-shaped domain, $p^i = p$, so that x_0 can be determined by a measurement of absolute pressure. In general flows, where $U \neq 0$, there is no systematic way of determining x_0 (even with a measurement of absolute pressure). Because GvH07's decomposition does not produce a unique value of internal-tide pressure, it is impossible to interpret physically. We are unaware of any published study that has attempted to use this decomposition to interpret internal-tide energy fluxes, except for KNK10. Choosing x_0 on the left- and right-hand sides of a numerical simulation, KNK10 found the decomposition produced depth-averaged pressure gradients and two different, but similarly unphysical, vertical profiles of energy flux (i.e., $u'p'$).

3.3 Assessing the Decompositions

KNK10 proposed several requisites for a successful surface/internal-tide decomposition. The first requisite required that the sum of the surface and internal tides equal the total flow. Both the decompositions of KNK10 and GvH07 comply with this requisite. The second requisite required that the definition of the internal tide adhere to the accepted normal-mode description of internal tides over a flat bottom (*Gill*, 1982). Indeed, the very idea of separating surface and internal tides is motivated by the property that, over a flat bottom, the 0th mode (i.e., the surface tide) produces most sea-surface displacement and propagates at a speed much faster than higher modes (i.e., the internal tide).

3.4 Application to Wedge Modes

The analytical solutions for waves in a wedge-shaped domain (*Wunsch*, 1968, 1969) provide an opportunity to compare internal-tide pressures p' (KNK10) and p^i (GvH07). As stated earlier, assuming a priori that these waves are purely internal tides implies that we already know how to identify internal-tide pressure. Therefore, we will assess the validity of p' and p^i by examining their compatibility with the normal-mode description of internal-tide pressure over a flat bottom. Fortunately, *Wunsch* (1968) outlined a method for matching flat regions to his solution on a slope. Including a continental shelf and abyssal plane (i) avoids the singularity in the solution at the wedge apex, (ii) better approximates the shape of a continental slope, and (iii) provides flat regions to compare p' and p^i with the normal-mode description of internal-tide pressure.

The general solution for pressure is

$$
p = \begin{cases} p_{flat} & x < x_1 \\[2mm] p_{slope} & x_1 < x < x_2 \\[2mm] p_{flat} & x > x_2 \end{cases} \quad , \tag{3.6}
$$

where the shelf-break is at $x = x_1$ and the abyss begins at $x = x_2$. The solution over the slope is

$$
p_{slope} = \hat{p} \sin \left[q \log \left(cx - z \right) \right] + \hat{p} \sin \left[q \log \left(cx + z \right) \right] + p_0 \tag{3.7}
$$

where $\hat{p}$ is an arbitrary amplitude and p_0 is an undetermined constant associated with horizontally integrating velocity. The parameters are $c = \omega^2 / N^2$, where ω is tidal frequency and N is buoyancy frequency; and $q = 2\pi n / \log \Delta$, where n is mode number, $\Delta = (c + \gamma) / (c - \gamma)$, and γ is the topographic slope.

The solution over a flat bottom is

$$
p_{flat} = \hat{p} \sum_{n=1}^{\infty} \cos \left(\frac{n\pi}{h} z \right) \left[a_n \cos \left(\frac{n\pi c}{h} x \right) - b_n \sin \left(\frac{n\pi c}{h} x \right) \right]
$$

$$
+ \left\langle p_{slope} \right\rangle |_{x=x_1 \text{ or } x_2} \tag{3.8}
$$

where a_n and b_n are determined by Cauchy boundary conditions at $x = x_1$ (shelf) or $x = x_2$ (abyss) (see *Wunsch*, 1968, for details).

One property of (3.8) is that depth-averaged pressures over the slope $\langle p_{slope} \rangle$ at $x = x_1$ and $x = x_2$ determine depth-averaged pressures over the shelf and abyss, respectively. Because p_{slope} has only one undetermined parameter p_0, p_{slope} can not generally be tuned

so that it has zero depth-average at both $x = x_1$ and $x = x_2$. Therefore, defining p^i as total pressure (GvH07) is incompatible with the normal-mode description of internal tides over a flat bottom.

A specific example where p^i violates the normal-mode description over a flat bottom is illustrated when $c = 0.6$, $\gamma = 0.5$, $n = 1$, $p_0 = 0$, and a shelf-break that occurs at $x = 8$ and an abyss that occurs at $x = 20$ (Fig. 3.1). We note that any configuration of shelf/slope/abyss produces similar results. Depth-average pressure is non zero on both sides of the slope, producing a depth-average pressure gradient. KNK10 interpret this flow as having internal-tide pressure p' (Fig. 3.1b) and non-zero surface-tide pressure P (Fig. 3.1a, black line). Since depth-averaged internal-tide pressure p' is always zero (by definition), it is compatible everywhere with the normal-mode description of internal tides over a flat bottom (Fig. 3.1a, red line). Conversely, GvH07 interpret this flow as having zero surface-tide pressure p^s (Fig. 3.1c, black line) and non-zero internal-tide pressure p^i (Fig. 3.1d). Since depth-average internal-tide pressure $\langle p^i \rangle$ is nonzero over both flat regions, this decomposition is incompatible with the normal-mode description of internal tides over a flat bottom (Fig. 3.1b, red line). Pink shading in Fig 3.1c represents those regions where GvH07's decomposition violates the accepted definition of internal-tide pressure over a flat bottom (*Gill*, 1982).

3.5   Conclusions

The correct choice for internal-tide pressure is p' because it is compatible with the accepted definition of internal-tide pressure over a flat bottom. Therefore, the correct internal-tide momentum equation is (3.3). For waves in a wedge-shaped domain, this equation indicates that the internal-tide produces wave-drag via a pressure perturbation along the

sloping bottom boundary. Because *Wunsch* (1968, 1969) constrained his solutions to have $U = 0$, wave-drag is counter-balanced by a surface-tide pressure gradient in the surface-tide momentum equation.

Defining p^i as internal-tide pressure, as suggested by GvH07, produces a confusing description of tidal dynamics. In their decomposition, the surface and internal-tide momentum equations are not coupled, and internal-tide pressure depends on an unknown limit of integration, usually making it impossible to determine uniquely. Practically speaking, the lack of wave drag makes it impossible for this decomposition to accurately represent the surface tide, even without a rigid lid (e.g., *Jayne and St. Laurent*, 2001; *Arbic et al.*, 2010). More confounding is that defining p^i as internal-tide pressure produces internal-tides with non-zero depth-average over a flat bottom, incorrectly suggesting that internal tides partially propagate as surface tides.

Acknowledgments
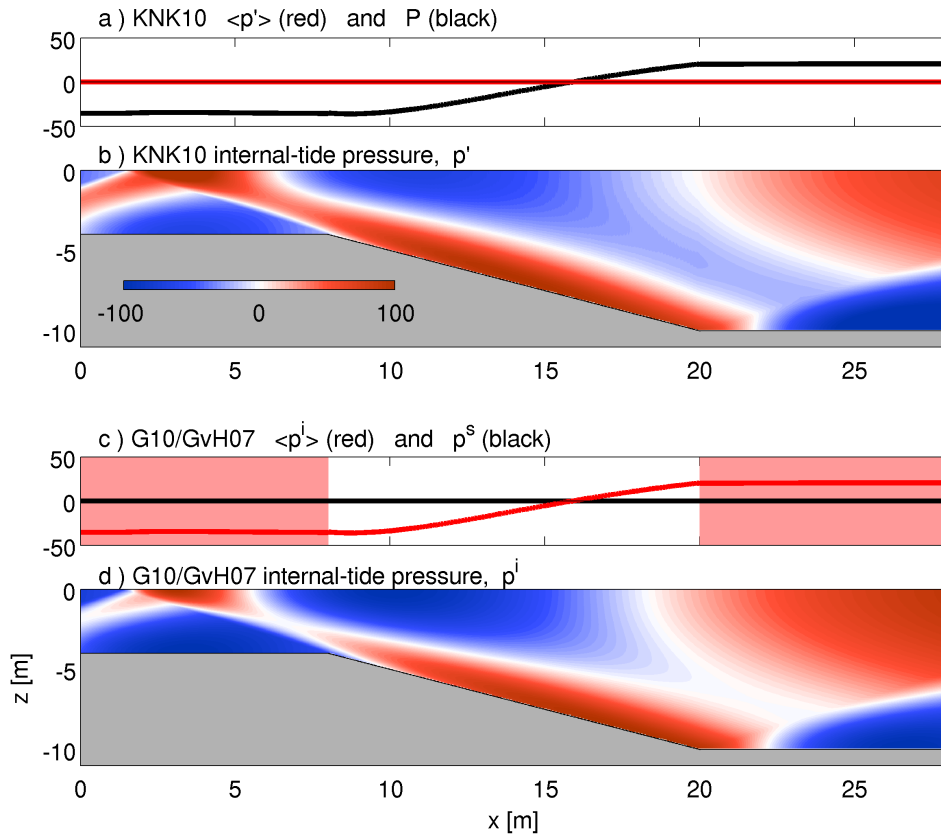
Figure 3.1: Surface and internal-tide pressure for wedge modes connected to a continental shelf and abyssal plane. (a) Surface-tide pressure P (black) and depth-averaged internal-tide pressure $\langle p' \rangle$ (red) (KNK10). (b) Internal-tide pressure p' (KNK10). (c) Surface-tide pressure p^s (black) and depth-averaged internal-tide pressure $\langle p^i \rangle$ (red) (GvH07). Red shading indicates that p^i is locally incompatible with flat-bottom modes. (d) Internal-tide pressure p^i (GvH07). Pressure amplitude $\hat{p}$ is defined so that total pressure varies between -100 and 100.

4. INTERNAL-TIDE GENERATION AND DESTRUCTION BY SHOALING INTERNAL TIDES

Samuel M. Kelly and Jonathan D. Nash

Abstract

Internal-tide generation is usually predicted from local topography, surface tides, and stratification. However, internal tides are often observed to be unrelated to local spring-neap forcing, appearing intermittently in 3-5 day bursts. Here we suggest a source of this intermittency by illustrating how remotely-generated shoaling internal tides induce first-order changes in local internal-tide generation. Theory, numerical simulations, and observations show that pressure perturbations associated with shoaling internal tides can correlate with surface-tide velocities to generate or destroy internal tides. Where shoaling internal tides have random phase, such as on the New Jersey slope, time-averaged internal-tide generation is unaffected, but instantaneous internal-tide generation varies rapidly, altering internal-tide energy and possibly affecting nonlinear internal waves, across-shelf transport, and mixing. Where shoaling internal tides are phase-locked to the local surface tide, such as in double-ridge systems, time-averaged internal-tide generation is affected and may result in resonance.

4.1   Motivation

Internal (i.e., baroclinic) tides are generated where surface (i.e., barotropic) tides force stratified fluid to flow up and over sloping topography (*Garrett and Kunze*, 2007), extracting 0.7 ± 0.15 TW of energy from the surface tide (*Egbert and Ray*, 2000) and contributing to mixing that maintains the abyssal density distribution (*Munk and Wunsch*, 1998). Along continental margins, internal tides drive sediment resuspension (*Butman et al.*, 2006), across-shelf transport (*Shroyer et al.*, 2010), and ecological processes (*Sharples et al.*, 2009).

Near major isolated topography such as the Hawaiian Ridge (*Rudnick et al.*, 2003),

vertical heaving by the surface tide dominates the displacement of isopycnals, producing "coherent" internal tides that are phase-locked with local surface tides. Variability of internal-tide generation at such sites is largely explained by local spring-neap cycles in surface-tide forcing and changes in background stratification. Because these parameters are fairly predictable, previous studies have estimated global maps of quasi-steady internal-tide generation (e.g., *Nycander*, 2005). These are supported by satellite observations, which resolve radiating internal tides that are coherent with the surface tide (*Ray and Mitchum*, 1996).

In-situ observations paint a different picture of the predictability of internal tides. These observations reveal that internal tides are intermittent and often uncorrelated with local spring-neap forcing (*Wunsch*, 1975). Supporting evidence is common along continental margins, e.g., the California Bight (*Lerczak et al.*, 2003), Mozambique Channel (*Manders et al.*, 2004), North Carolina Shelf (*Savidge et al.*, 2007), Portuguese Shelf (*Sherwin et al.*, 2002), and Virginia Slope (*Nash et al.*, 2004).

Intermittent motions that are not phase-locked to the surface tide are termed "incoherent" (*van Haren*, 2004) and are spectrally manifested as a wide peak around the tidal frequency. Incoherence can arise as internal tides transit thousands of kilometers through mesoscale currents and stratification (*Zhao and Alford*, 2009), which alter their propagation speed and direction (*Rainville and Pinkel*, 2006), and cause their phase upon reaching distant locations to wander. Incoherence in observations of internal tides may therefore indicate the presence of remotely-generated internal tides.

Along continental margins, an idealized internal tide can be represented as a linear

superposition of a locally-generated and remotely-generated shoaling internal tide:

$$u' = u'_{local} + u'_{shoal} \qquad \text{and} \qquad p' = p'_{local} + p'_{shoal}$$

where, u' and p' are internal-tide velocity and pressure (i.e., they have zero depth-average, *Kunze et al.* (2002)). Conceptually, the locally-generated internal tide is forced by, and coherent with, the local surface tide, whereas the shoaling internal tide is forced by a remote surface tide, and may or may not be coherent with the local surface tide (Fig. 4.1). In the following investigation, we examine the way in which shoaling internal tides impact internal-tide generation. We suggest that these dynamics explain some 3-5 day variability in internal-tide energy along continental margins.

4.2 Decomposing Internal-Tide Generation

Internal-tide generation (sometimes referred to as topographic energy conversion) quantifies the rate of work per unit area on the internal tide by the surface tide. Over arbitrary topography, the linear limit for internal-tide generation is:

$$C = \nabla H \cdot \overline{\mathbf{U}p'}|_{z=H} \quad [\text{W/m}^2] \tag{4.1}$$

where $\mathbf{U}$ is surface-tide velocity, an overbar indicates a tidal average, $z = H$ defines the bottom, and ∇H is the topographic gradient (*Kurapov et al.*, 2003).

In this section we use four hydrodynamic simulations with idealized forcing to isolate internal-tide generation due to surface and shoaling-internal tides, i.e., $C = C_{local} + C_{shoal}$. Numerical simulations are conducted with the MIT general circulation model (*Marshall et al.*, 1997) in a two-dimensional domain with 25-m horizontal and 5-m vertical resolution;

planetary rotation is zero, buoyancy frequency is constant (ten times the semidiurnal frequency), and horizontal and vertical eddy viscosities are constant (10^{-1} and 10^{-2} m^2/s, respectively). Semidiurnal forcing is applied at the boundaries and sponge conditions prevent reflection of outward-radiating internal tides. Continental-slope topography is half-Gaussian with a maximum slope that is supercritical with respect to a semi-diurnal internal-tide characteristic.

When a surface tide is prescribed without a shoaling internal tide (BT sim.; Fig. 4.2, leftmost column), all internal-tide pressure results from the displacement of isopycnals as the surface tide encounters topography, i.e., $p' = p'_{local}$ (Fig. 4.2a). Local internal-tide generation,

$$C_{local} = \nabla H \cdot \overline{\mathbf{U} p'_{local}}|_{z=H} , \tag{4.2}$$

is positive (Fig. 4.2i) and produces internal tides with energy fluxes ($F_E = \overline{u'p'}$, *Kunze et al.* (2002)) that radiate away from the slope (Fig. 4.2e). C_{local} depends only on local topography, surface-tide forcing, and background stratification.

In contrast, when a shoaling internal tide is prescribed without a surface tide (BC sim; Fig. 4.2, middle-left column), internal-tide pressure is produced entirely by the shoaling internal tide, i.e., $p' = p'_{shoal}$ (Fig. 4.2b). The resulting net internal-tide energy flux is onshore (Fig. 4.2f) because the shoaling internal-tide is partially transmitted onto the continental shelf and partially reflected to the deep ocean. In this case,

$$C_{shoal} = \nabla H \cdot \overline{\mathbf{U} p'_{shoal}}|_{z=H} \tag{4.3}$$

is approximately zero (Fig. 2j), because $\mathbf{U} \approx 0$.

In two cases that more closely resemble continental margins, surface and shoaling internal tides are prescribed simultaneously (BT+BC sims. 1 and 2). Internal-tide

generation now contains contributions from both C_{local} and C_{shoal}. C_{local} is identical to the case with only surface tides. However, C_{shoal}, unlike the case with only shoaling internal tides, is no longer zero because $\mathbf{U} \neq 0$.

In the presence of surface and shoaling internal tides C_{shoal} can be positive (BT+BC sim. 1; Fig. 4.2, middle-right column) or negative (BT+BC sim. 2; Fig. 4.2, rightmost column), depending on the phasing of surface tide velocity U and internal-tide bottom pressure $p'|_{z=H}$. When U and $p'|_{z=H}$ have positive covariance (BT+BC sim. 1; Fig. 4.2c), the slope strongly radiates internal-tide energy (Fig. 4.2g). In this case, $C_{shoal} > 0$, indicating additional energy is extracted from the surface tide (Fig. 4.2k). Alternatively, when the phase of the shoaling internal tide is shifted by $180°$ (BT+BC sim. 2), U and $p'|_{z=H}$ have negative covariance (Fig. 4.2d), and the slope weakly radiates internal-tide energy (Fig. 4.2h). In this case, $C_{shoal} < 0$, indicating internal-tide energy is lost to the the surface tide (Fig. 4.2l), a process we term internal-tide destruction. *Kurapov et al.* (2003) identified $C < 0$ in numerical simulations and similarly associated it with remotely-generated internal tides. Internal-tide destruction is analogous to energy transfer from near-inertial waves to surface winds that oppose wave motion (*D'Asaro*, 1985).

Thus, internal-tide generation depends on the phases and amplitudes of shoaling internal tides as well as local topography, surface tides, and stratification. Since shoaling internal tides depend on forcing at their origins, plus mesoscale variability (which influences their propagation), internal-tide generation is a global-scale phenomena. Furthermore, coupling between distant locations can occur because shoaling internal tides at one location are influenced by shoaling internal tides at their origins.

4.3 Incoherent Shoaling Internal Tides

In the analysis of observations, it is often impossible to isolate p'_{shoal}. If it is assumed that shoaling internal tides have random phase, then p'_{shoal} can be estimated by identifying the component of p' that is incoherent with the local surface tide. This represents a lower bound on p'_{shoal} because an additional portion of the shoaling internal tide may be coherent with the local surface tide (Section 4.4).

Here, we examine coherence in observations from the New Jersey slope (*Shroyer et al.*, 2010) to separate the locally-generated and shoaling internal tides. These observations were collected in the summer of 2006 from three moorings that recorded full-depth profiles of velocity and density. Coherent signals are extracted from band-passed records (which retain 4-30 hour variability) using least-squares harmonic regression to nine tidal frequencies. During the 40-day record, the coherent internal tide (computed as the difference between the band-passed and coherent timeseries) is modulated by the local spring-neap cycle and has divergent energy flux (Fig. 4.3a and b). Conversely, the incoherent internal tide is intermittent, but contains no spring-neap variability and always produces onshore energy flux. We therefore associate coherent pressure and velocity with a locally-generated internal tide, and incoherent pressure and velocity with a shoaling internal tide.

To illustrate the importance of the shoaling tide's phase, we examine C during a 7-day period in the middle of the record. During this period, p'_{local} is almost completely in phase with $\mathbf{U}$ (Fig. 4.3c) so that C_{local} is maximized and varies slowly with the spring-neap cycle (Fig. 4.3e, red). Conversely, p'_{shoal} drifts in and out of phase with $\mathbf{U}$ (Fig. 4.3d, blue) so that C_{shoal} varies on a 3-5 day timescale and is both positive and negative (Fig. 4.3e).

Around 16 August, constructive phasing between p'_{shoal} and $\mathbf{U}$ (Fig. 4.3d) produces a peak in total internal-tide generation (Fig. 4.3e) that is not explained by local spring-neap

forcing or background stratification. Three days later, destructive phasing arrests internal-tide generation. These events are manifested in the record of internal-tide energy-flux divergence at the shelf break (Fig. 4.3f), which is quantitatively consistent with internal-tide generation and destruction (Fig. 4.3e), and indicates that the slope transitions from a 400 W/m source to a 200 W/m sink in just three days (Fig. 4.3a and b). The timing of this transition, which occurs over a third of the spring-neap cycle, is dictated entirely by the phasing between p'_{shoal} and $\mathbf{U}$.

Because incoherent internal tides have random phase, they modulate instantaneous internal-tide generation, but do not affect its time average. While local models can estimate time-average C, they can not predict episodic bursts in C_{shoal} (and F_E), which may influence mixing, sediment resuspension, across-shelf transport, and other processes that are nonlinear functions of internal-tide energy.

4.4 Coherent Shoaling Internal Tides

Shoaling internal tides can also be coherent with the local surface tide (*Colosi and Munk*, 2006). When a shoaling internal tide is weakly affected by mesoscale variability, it arrives at the same phase each tidal period producing constant C_{shoal}. In double-ridge systems, such as within the Luzon Strait, internal-tide generation can be sensitive to topographic spacing and stratification (*Echeverri and Peacock*, 2010) because of coherent shoaling internal tides. Resonance occurs when time-averaged C_{shoal} is positive and the newly-generated internal tide propagates to the generation site of the original shoaling tide, producing positive C_{shoal} there and initiating an endless loop of intensification. For topographic features of limited spatial extent, resonance has been investigated using ray theory to identify internal-wave attractors (e.g., *Maas et al.*, 1997; *Tang and Peacock*, 2010). Ray theory is less applicable

to basin-scale topography where high-mode internal tides are rapidly attenuated.

In addition, low-mode internal tides are observed to propagate thousands of kilometers, and their shoaling can induce the generation of subsequent low-mode internal tides. *Dushaw and Worcester* (1998) reported observations of a K1 internal tide resonating between Puerto Rico and the turning latitude, 1100 km to the North. They recognized an increase in internal-tide generation but did not propose a mechanism. We speculate that C_{shoal} was positive and increasing with each reflection.

4.5   Consequences

Here we have shown that remotely-generated shoaling internal tides produce first-order changes in local internal-tide generation. The sign and magnitude of C_{shoal} depends on the correlation between surface-tide velocity and shoaling internal-tide pressure. Incoherent shoaling internal tides alter instantaneous internal-tide generation, while coherent shoaling internal tides alter time-averaged internal-tide generation.

Historically, estimates of internal-tide generation have ignored shoaling internal tides by calculating generation completely from local forcing (e.g., *Nycander*, 2005). Because these models can misrepresent time-averaged internal-tide generation (when internal tides are coherently shoaling), global models that include internal-tide propagation, dissipation, and shoaling (e.g., *Arbic et al.*, 2010) will eventually provide the best estimates of internal-tide generation. Unfortunately, global models with weakly damped internal tides may prove inherently chaotic because shoaling internal tides at one location are determined in part by shoaling internal tides at their places of origin. Until models with realistic internal-tide dissipation converge on a time-averaged map of internal-tide generation, satellite-derived estimates of surface-tide losses (*Egbert and Ray*, 2000) may provide the most reliable

estimates of time-averaged internal-tide generation.

More importantly, neither local nor global models can currently predict short-term variability in internal-tide generation. Episodic bursts in internal-tide energy and energy flux are likely to impact nonlinear mass, momentum, nutrient, and larval transports. In many locations, in-situ observations provide the only first-order accurate estimates of instantaneous internal tides.

4.6   Appendix A: Energy Flux on the Continental Shelf (Unpublished)

In the numerical simulations presented in Section 4.2, the phasing of velocity and pressure are found to effect internal-tide energy flux on the continental shelf (Fig. 4.4). When the locally-generated internal tide (Fig. 4.4, a and b) is combined with the remotely-generated internal tide (Fig. 4.4, c and d) the superposition either enhances (Fig. 4.4, e and f) or suppresses (Fig. 4.4, g and h) onshore internal-tide energy flux. In BT+BC sim. 2, the internal tide is energetic enough to exhibit nonlinear dynamics (i.e., wave steepening). These simulations suggest that shoaling internal tides may influence nonlinear internal-wave generation on some continental shelves. For instance, shoaling internal tides may be important on the New Jersey Shelf, where nonlinear internal-wave generation is not strongly linked to local spring-neap forcing (*Moum and Nash*, 2008; *Nash et al.*, 2010).

4.7   Appendix B: Two-Slope Resonance (Unpublished)

To examine the possibility of resonant internal-tide generation, several numerical simulations were conducted with surface-tide forcing and a second opposing continental slope (Fig. 4.5). To identify the role of spacing, the base of the second slope was placed

2.25, 2.5, 2.75, and 3 mode-1 wavelengths from that of the original slope. Internal-tide generation was found to change drastically with the position of the second slope. At 3 mode-1 wavelengths, internal-tide generation was almost completely suppressed. At 2.75 mode-1 wavelengths, internal-tide generation (over just the original slope) more than doubled the value for a single-slope system.

Resonant internal-tide generation between double ridges has been examined by *Echeverri and Peacock* (2010), who employed semi-analytical methods to calculate internal-tide generation. Here, we suggest that although exact resonate solutions may be sensitive to three-dimensional effects, viscosity, topography and stratification, the importance of internal-tide generation by shoaling internal tides is robust. Specifically, although a two-slope system may drift in and out of resonance, internal-tide generation will always be effected, to first-order, by the existence of a second slope.

Acknowledgments
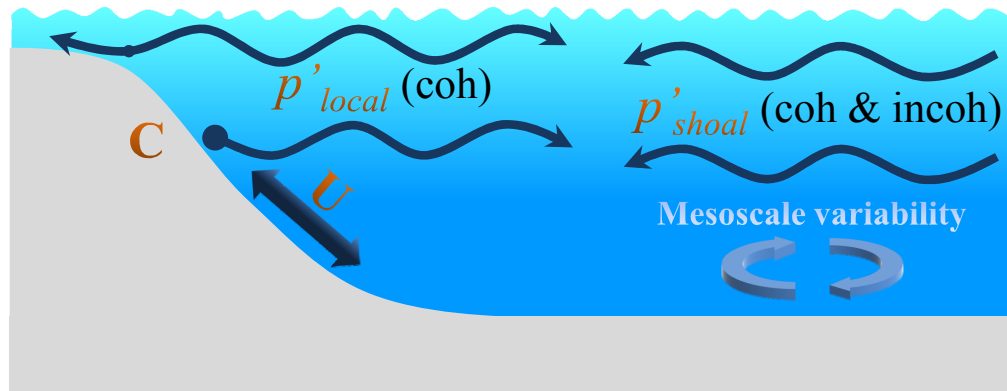
Figure 4.1: Internal tides on a continental slope. On the left, the surface tide $\mathbf{U}$ is deflected by the slope and produces pressure perturbations p'_{local} that are coherent with $\mathbf{U}$. On the right, internal tides with pressure perturbation p'_{shoal} impinge on the slope. p'_{shoal} may, or may not, be coherent with $\mathbf{U}$, as the propagating tides are scrambled by mesoscale features. Internal-tide generation C occurs along the sloping bottom and depends on how $\mathbf{U}$ covaries with p'_{local} and p'_{shoal}.
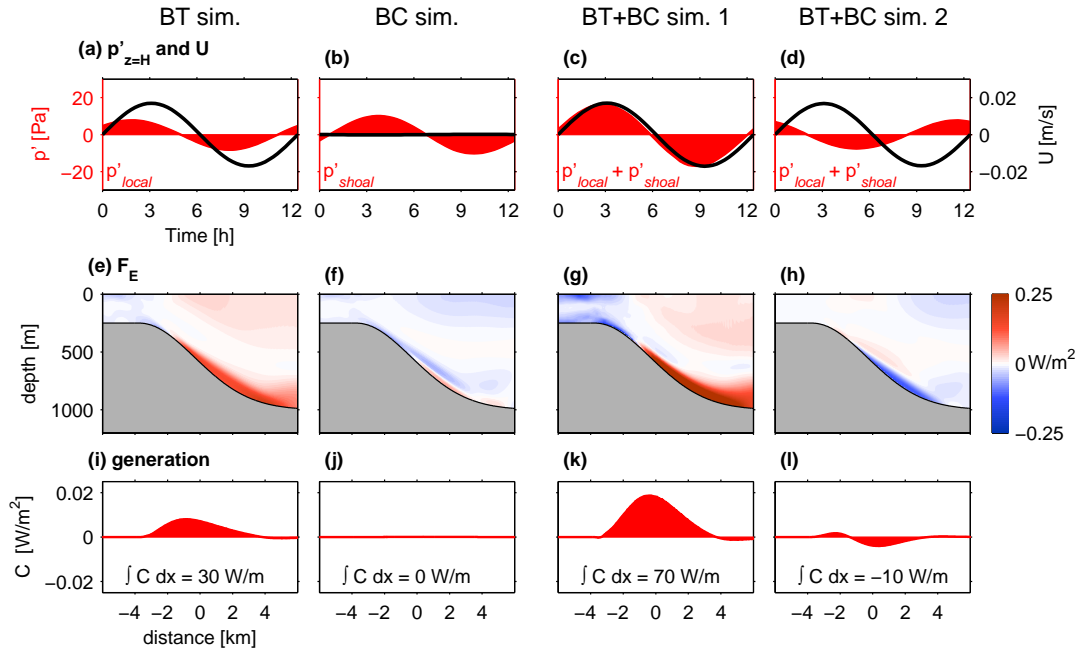
Figure 4.2: Four simulations of internal-tide generation. Columns from left to right: BT sim. is forced by a surface tide. BC sim. is forced by a shoaling mode-1 internal-tide. BT+BC sim. 1 is forced by surface and shoaling internal tides that are phased to maximize internal-tide generation. BT+BC sim. 2 is identical to BT+BC sim. 1, except the shoaling internal tide is phase shifted by 180° to minimize internal-tide generation. (a-d) Timeseries of internal-tide bottom pressure and surface-tide velocity at $x = 0$ km. The amplitudes and phasing of $\mathbf{U}$ and p' determines internal-tide generation. (e-h) Internal-tide energy flux. (i-l) Internal-tide generation and its horizontal integral.
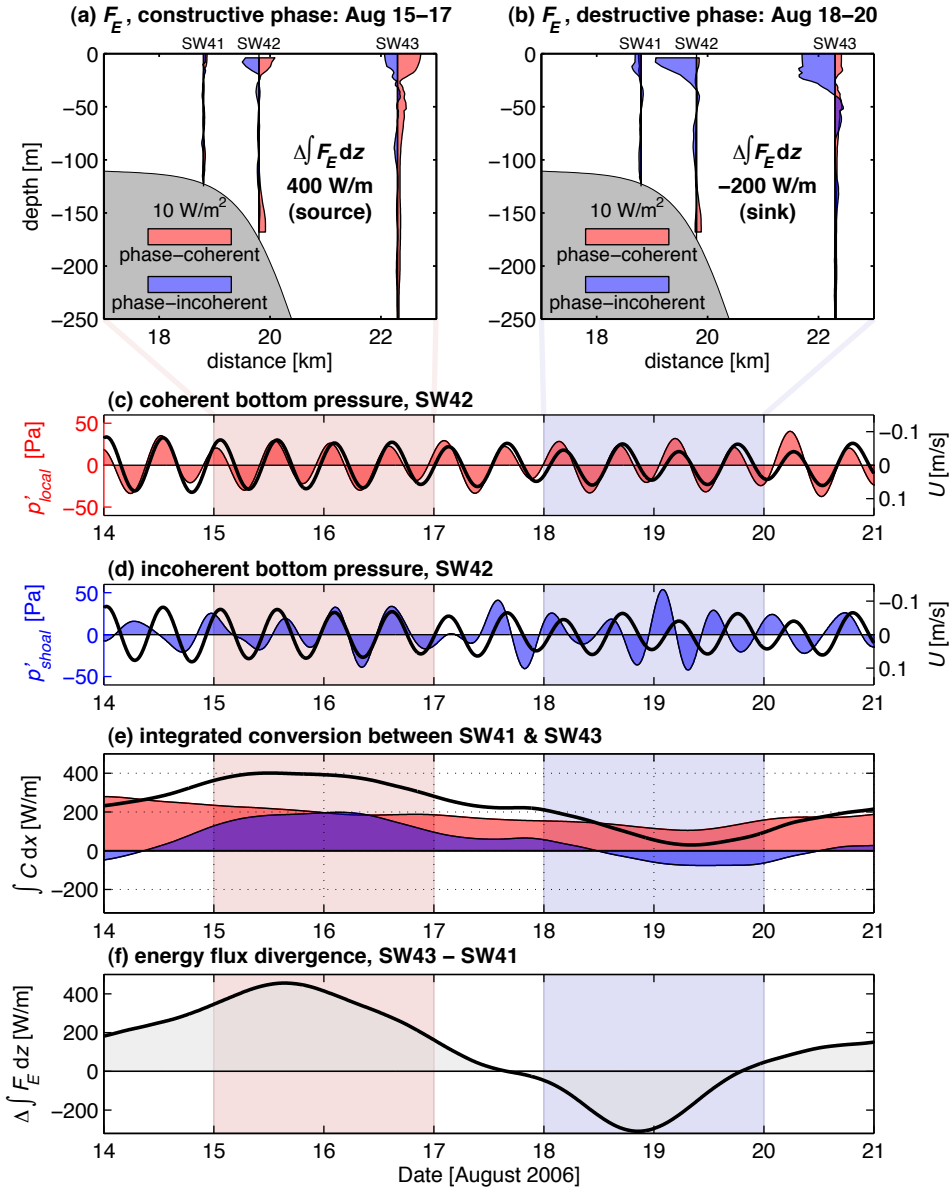
Figure 4.3: Observations from the New Jersey continental slope. (a and b) Coherent energy flux $\overline{u'_{local}p'_{local}}$ (red) is offshore, while incoherent energy flux $\overline{u'_{shoal}p'_{shoal}}$ (blue) is onshore. Total energy-flux divergence (which includes cross-terms) is indicated, and determines whether the slope is a source or sink of internal-tide energy. (c) p'_{local} (red) and $\mathbf{U}$ (black) are in phase throughout the record. (d) p'_{shoal} (blue) and $\mathbf{U}$ (black) drift in an out of phase. (e) As a result, integrated C_{local} (red) varies slowly in accordance with the local spring-neap cycle while C_{shoal} (blue) varies on a 3-5 day timescale. (e) Total internal-tide generation (black) and (f) energy-flux divergence (black) are quantitatively similar and significantly modified by C_{shoal}. Integrated C is calculated from 2-km smoothed topography and the trapezoidal rule.
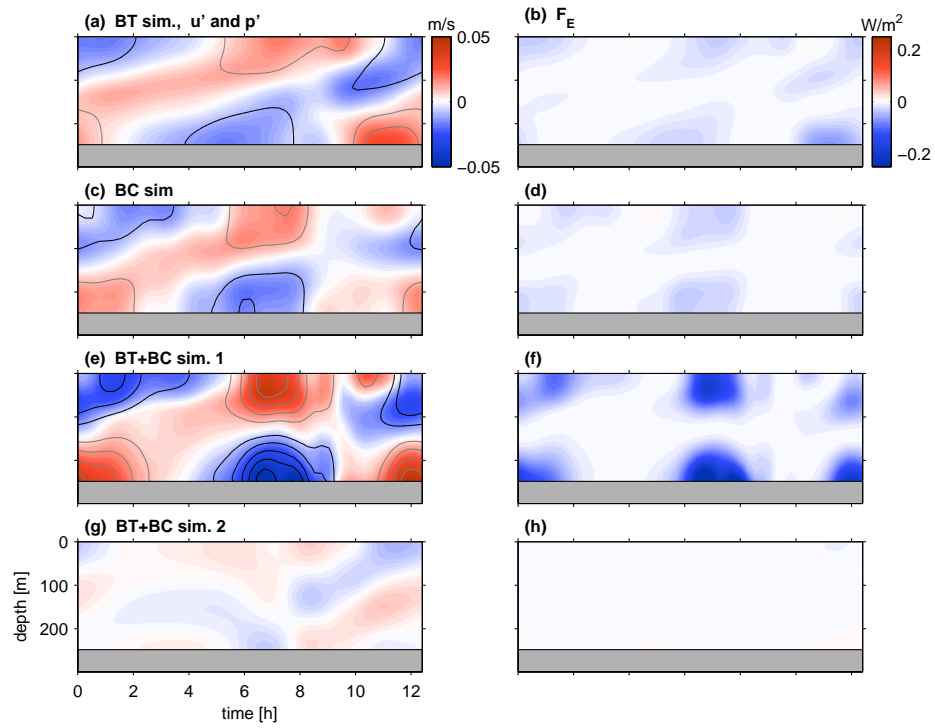
Figure 4.4: Timeseries of internal-tide energy flux on the continental shelf ($x = -5$ km). Left-column: Internal-tide velocity (color) and pressure (contours) for the (a) BT sim., (c) BC sim., (e) BT+BC sim. 1, and (g) BT+BC sim. 2. Pressure contours are every 5 Pa; black contours are positive, gray contours are negative. Right-column: (b, d, f, and h) Internal-tide energy flux (blue is onshore).
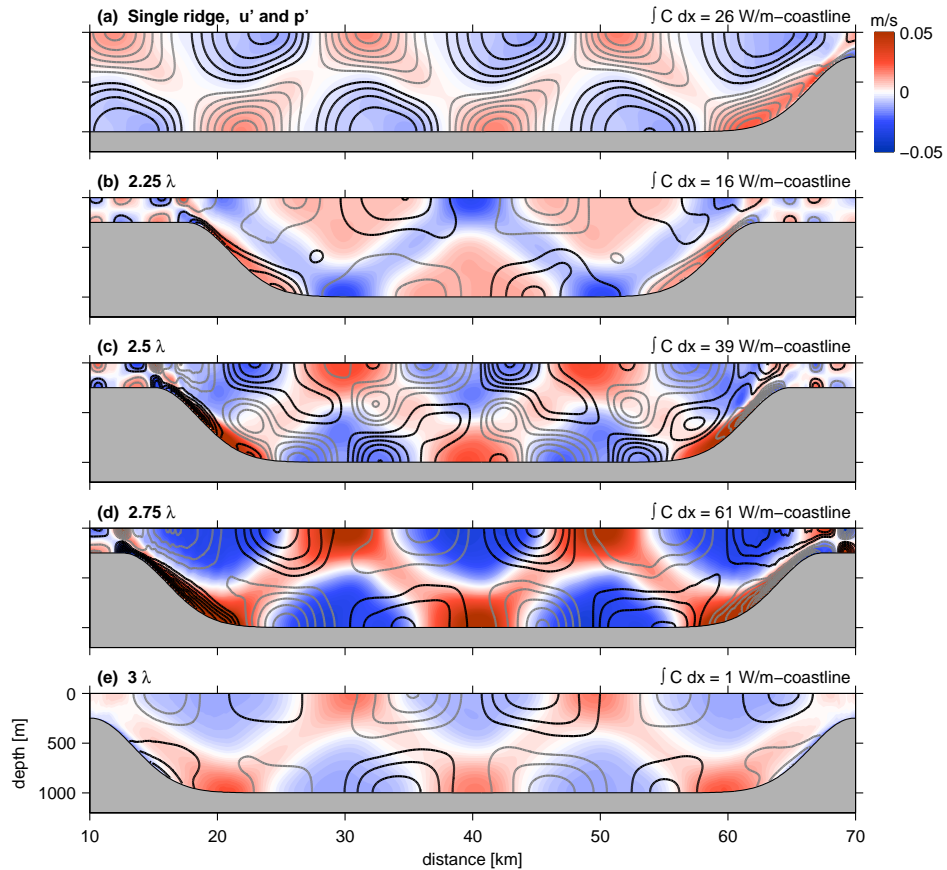
Figure 4.5: Internal-tide resonance in a two-slope system with surface-tide forcing. Internal-tide velocity (color) and pressure (contours) for (a) a single-slope system and two-slope systems with (b) 2.25, (c) 2.5, (d) 2.75, and (e) 3 mode-1 wavelengths between bases. Pressure contours are every 5 Pa; black contours are positive, gray contours are negative. Internal-tide generation over the right slope is given on the right-hand side of each panel.

5. TIDE-TOPOGRAPHY COUPLING ON A CONTINENTAL SLOPE

Samuel M. Kelly, Jonathan D. Nash, Kim. I. Martini, Matthew H. Alford, and Eric Kunze

Abstract

Observations of the semidiurnal internal tide on the Oregon slope indicate 500 W/m-coastline of (i) surface-tide energy loss and (ii) turbulent kinetic energy dissipation. Comparison with numerical simulations suggest the observed internal tide is a superposition of locally-generated and shoaling internal tides. Here, we derive a new expression for linear tide-topography coupling, which includes both internal-tide generation and scattering. Quantifying these terms, we find that surface-tide energy loss and turbulent kinetic energy dissipation are consistent with two observed forms of tide-topography coupling. Next, we estimate onshore and offshore energy fluxes, which confirm the presence of locally-generated and shoaling internal tides and suggest the importance of 3-D dynamics. The results of this study indicate that shoaling internal tides are unlikely to survive reflection from continental slopes and tide-topography coupling may contribute significantly to deep-ocean tidal-energy dissipation.

5.1   Introduction

Munk (1966) suggested that tidally-driven mixing in the deep ocean may be important for maintaining abyssal stratification. An ensuing challenge has been to identify the deep-ocean distribution of tidal-energy dissipation. *Egbert and Ray* (2001) mapped surface-tide energy loss, but most surface-tide energy is converted to low-mode internal-tides (*Garrett and Kunze*, 2007), which are observed to propagate O(1000 km) (*Ray and Mitchum*, 1996) before dissipating.

Tides have historically been described as a linear superposition of uncoupled normal modes (*Wunsch*, 1975). However, because the astronomical tide-generating force only acts

on the surface tide (mode 0) (*Hendershott*, 1981), some form of modal coupling is required to power the observed internal tides (modes $n \geq 1$). *Zeilon* (1912) demonstrated topographic internal-tide generation in laboratory experiments, but it was not until *Rattray* (1960) that the first mathematical description of tide-topography coupling was published.

More recently, observations (e.g., *Rudnick et al.*, 2003) and global tide models (e.g., *Jayne and St. Laurent*, 2001) have demonstrated that surface-tide energy losses in the deep ocean are predominately due to internal-tide generation, which can be approximated by linear dynamics where surface-tide excursions are small (*Garrett and Kunze*, 2007). Mathematically, linear internal-tide generation can be written as a generic expression, C (Section 5.5.1), which has been verified in numerical simulations (e.g., *Niwa and Hibiya*, 2001; *Kurapov et al.*, 2003; *Carter et al.*, 2008) and observations (*Kelly and Nash*, 2010).

Tide-topography coupling may also explain energy losses from the low-mode internal tides. Theory and observations suggest that low-mode internal tides are dissipated during reflection and scattering at continental margins (*Eriksen*, 1998; *Nash et al.*, 2004, 2007; *Alford and Zhao*, 2007), but not during propagation in the open ocean (*St. Laurent and Garrett*, 2002; *Alford et al.*, 2007). In addition, numerical simulations have demonstrated that tide-topography coupling efficiently scatters low-mode internal tides to higher modes (*Johnston and Merrifield*, 2003; *Johnston et al.*, 2003), which may subsequently dissipate locally (*St. Laurent and Garrett*, 2002; *Muller and Bühler*, 2009). Unfortunately, it has been difficult to quantify the importance of tide-topography coupling without a general mathematical expression for internal-tide scattering. In Section 5.5.1, we derive such an expression, $C_{m,n}$, which like C is valid where ever tidal excursions are small.

If tide-topography coupling is the primary mechanism for low-mode internal-tide energy losses, continental margins, which catch much of the radiating internal tide, could be the location of most deep-ocean tidal-energy dissipation. In the present study, we examine

observations and numerical simulations of tidal dynamics on the Oregon continental slope at 43.2° N (which is steep, rough, turbulent (*Moum et al.*, 2002) and characteristic of western North America, Fig. 5.1). Here, *Egbert and Ray* (2001) infer 500 W/m-coastline of surface-tide energy loss, which we associated with internal-tide generation (Fig. 5.2), and *Nash et al.* (2007) observe 500 W/m-coastline of tidally-modulated near bottom turbulent kinetic-energy dissipation, which we associate with tidal-energy dissipation. In addition, *Martini et al.* (2011b) present evidence that shoaling internal tides transform into near-bottom turbulent bores at stations MP3 and MP4 (Fig. 5.1, b), driving turbulent kinetic-energy dissipation.

Despite estimates of net internal-tide generation and dissipation, characterizing internal-tide dynamics on the Oregon slope has been difficult because of the simultaneous presence of locally-generated and shoaling internal tides. Examining 40-day mooring records, *Martini et al.* (2011a) identify intermittent periods of net onshore and offshore internal-tide energy fluxes and complex interference patterns. Here, we complement *Martini et al.* (2011a), by comparing observations over a brief 2-day period with 3-D numerical simulations of internal-tide generation and shoaling. The goals of this investigation are to (i) identify the presence of locally-generated and shoaling internal tides, (ii) quantify internal-tide generation and compare it with observed surface-tide energy loss, and (iii) quantify the conversion of tidal energy into high modes and compare it with observed turbulence.

The remainder of the paper is organized as follows: In Section 5.2, we present an observational snapshot of the semidiurnal internal tide's structure across the Oregon slope. In Section 5.3, we present two three-dimensional numerical simulations of tidal dynamics on the Oregon slope. One simulation is designed to isolate local internal-tide generation, the other mode-1 internal-tide shoaling. In Section 5.4, we compare observed and simulated velocities and pressures, finding evidence of both locally-generated and shoaling internal

tides. In Section 5.5, we derive energy balances that include inter-modal energy conversion. We then quantify internal-tide generation and energy conversion to high modes, which we compare to surface-tide energy loss and turbulent dissipation, respectively. In Section 5.6, we estimate the amplitudes of onshore and offshore propagating internal tides, finding evidence for 3-D tidal dynamics. In Section 5.7, we review tidal energetics on the Oregon slope and consider the relevance of continental margins in the global tidal-energy balance.

5.2 Observations

During a spring tide in September 2005, the Oregon continental slope, which runs north-south, was sampled in ten locations at $43.212°$ N (Fig. 5.1, a and b). Sampling stations were spaced approximately 3 km apart, between the shelfbreak and abyssal plain, to produce a cross-slope picture of tidal dynamics. Three sampling schemes were employed to obtain almost full-water-column measurements (see also *Nash et al.*, 2007; *Martini et al.*, 2011a,b):

(i) At three locations, McLane Moored Profilers (MPs) continuously traversed the water column, obtaining vertical profiles of velocity, temperature, and salinity every 3 h or less over a 40-day deployment. (Two additional moorings, MP1 and MP6, are omitted from this analysis because their water-column coverage is inadequate for the vertical-mode decomposition described in Section 5.5.2.)

(ii) At six locations, eXpendable Current Profilers (XCPs) collected depth-profiles of velocity and temperature, during a 24-hour survey, while the ship steamed from station to station. XCP-measured velocities are relative to a depth-independent constant and are made absolute using GPS-referenced 75-kHz shipboard ADCP velocities between 20 and 300 m. Because XCPs do not measure conductivity, salinity was inferred from the unambiguous temperature-salinity relationships at nearby MPs and CTDs.

(iii) At one location, a CTD/Lowered-ADCP package (LADCP) was yo-yoed vertically over the side of the ship to obtain an 18-h timeseries of velocity, temperature, and salinity. (Several additional LADCP timeseries are omitted from this analysis because they were obtained several days earlier or later, during different conditions of surface tide and shoaling internal-tide forcing (*Martini et al.*, 2011a).)

In order to create an across-slope snap-shot of the semi-diurnal internal tide, MPs records were only analyzed during a 3-d window coincident with the XCP survey and LADCP station (Fig. 5.1c). While the 3-day MP records may include additional temporal variability, the strength of the surface tide is approximately constant over this spring-tide period, and the lengthened records reduce errors in semi-diurnal fits. Although LADCP measurements were taken several hours after the XCP survey, there inclusion provides valuable information about tidal dynamics on the lower-slope.

5.3   Numerical Simulations

Over the 40-day mooring records, *Martini et al.* (2011a) identified periods dominated by locally-generated and shoaling internal tides. However, during the period examined here, they concluded that both tides were present and difficult to deconvolve. To aid in our interpretation of these observations, we conduct two three-dimensional diagnostic numerical simulations with realistic 250-m topography (courtesy J. Chaytor and C. Goldfinger, *Romsos et al.*, 2007) and 20-m stratification. The generation simulation is forced at the boundaries by realistic surface-tide velocities (TPXO7.2 *Egbert*, 1997) to reproduce the locally-generated internal tide. The shoaling simulation is forced at the western boundary by an onshore (eastward) propagating internal-tide in lieu of a surface tide to approximate a shoaling internal tide.

Because the vertical structure, direction, amplitude, and phase of the true shoaling internal tide are not known a priori, we force the shoaling simulation in the simplest manner that is still relevant for interpreting observations. The prescribed vertical structure is mode-1 because it dominates observed energy flux (Section 5.5.4) and is associated with long-distance propagation (e.g., *Ray and Mitchum*, 1996). J. Klymak (personal communication) has found that prescribing an additional mode-2 shoaling wave can drastically alter the dynamics of mode-1 scattering. Here, we avoid this layer of complexity by prescribing a single mode-1 wave. The prescribed direction is eastward. Although *Martini et al.* (2011a) report similarities between observed energy fluxes and those of a northward-propagating obliquely-shoaling internal tide, an eastward propagating tide is less ambiguous to prescribe numerically because topography to the west is approximately flat. In addition, we expect a northward-propagating tide to refract in this direction as it shoals (like a surface wave on a beach). Finally, the prescribed phase and amplitude of the shoaling internal tide are chosen so that simulated velocity, pressure, and onshore energy flux are qualitatively similar to observations (i.e., onshore energy flux is approximately 500 W/m-coastline, Sections 5.4 and 5.5.4). Given the approximations required to force the shoaling simulation, we expect it to be illustrative rather than predictive.

Numerically, both simulations are conducted with the MIT general circulation model (MITgcm, *Marshall et al.*, 1997). The model is configured with a linear free surface, free-slip boundary conditions, f-plane planetary rotation, two-thousand time-steps per tidal period and constant eddy viscosities of 1×10^{-1} and 1×10^{-2} m^2/s in the horizontal and vertical, respectively. The eddy viscosities are large because we have simplified the model's energy balance by avoiding a complicated turbulence closure. The full model domain contains 400 $\times$ 240 $\times$ 155 points in the x, y, and z directions and ranges between 42.8-43.7° N and 124.2-127° W (Fig. 5.1, a). Horizontal resolution begins to telescope smoothly from 250 to 1000

m 25 km north and south of 43.2° N and over the abyssal plain. A flow-relaxation scheme is applied at the lateral boundaries to prevent the reflection of internal waves. We sample velocity, temperature, and salinity during the tenth tidal-cycle when the energy balance has reached an approximate steady state.

5.4   Velocity and Pressure

Because Oregon slope internal tides are dominantly large scale, velocity and pressure can be approximated as a linear superposition of locally-generated and shoaling wavefields. The observed structures of velocity and pressure contain qualitative similarities to both numerical simulations.

5.4.1   Theory

Large-scale tidal motions are dominated by linear, hydrostatic, mechanics. Combining the vertical-momentum, buoyancy, and continuity equations with these approximations, reduces the equations of motion to:

$$\begin{pmatrix} -i\omega & -f \\ f & -i\omega \end{pmatrix} \mathbf{u} = -\nabla p \tag{5.1}$$

$$\nabla \cdot \mathbf{u} = \left(\frac{p_{zt}}{N^2} \right)_z , \tag{5.2}$$

where $\mathbf{u}$ is horizontal velocity, p reduced-pressure perturbation, ω the tidal frequency, f the Coriolis frequency, N the buoyancy frequency, ∇ the horizontal gradient operator, and the domain extends between $z = [0, H(\mathbf{x})]$.

5.4.2   Methods

Temperature and salinity at each observational station are used to calculate depth-profiles of instantaneous (ρ) and tidally-averaged (ρ_0) density. Following *Desaubies and Gregg* (1981), ρ_0 is calculated as the average depth of each isopycnal rather than the average isopycnal at each depth. Internal-tide pressure is obtained from the hydrostatic balance by integrating buoyancy, $b = -g(\rho - \rho_0)/\rho_0$, and removing the depth-average:

$$p' = \int_0^z b \, \mathrm{d}z - \left\langle \int_0^z b \, \mathrm{d}z \right\rangle , \tag{5.3}$$

where $\langle \cdot \rangle$ denotes a depth average (*Kunze et al.*, 2002). Surface-tide pressure, which requires an absolute measurement of sea-surface displacement, is unknown in the observations and therefore not analyzed. *Kelly et al.* (2010) identified a depth-dependent component of surface-tide pressure, which arises from isopycnal heaving by movement of the free surface, and can lead to O(50 W/m-coastline) errors in internal-tide energy flux. We correct internal-tide pressures using surface-tide displacements from TPXO7.2 (*Egbert*, 1997) and *Kelly et al.* (2010)'s (27) and (28). Surface and internal-tide velocities are defined $\mathbf{u}_0 = \langle \mathbf{u} \rangle$ and $\mathbf{u}' = \mathbf{u} - \mathbf{u}_0$, respectively.

Semidiurnal fits to all available measurements of velocity and pressure are estimated over 50-m vertical intervals by least-squares regression. Results are scaled by $\sqrt{2}$ to produce concise notation for tidally-averaged kinetic energy ($\mathbf{u}^2/2$) and energy flux ($\mathrm{Re}[\mathbf{u}'^* p']$). Phases in the observations and generation simulation are referenced from the time of maximum northward surface-tide velocity. Phase in the shoaling simulation is defined to maximize qualitative similarities with the observations. To limit the introduction of error, phases are not reported where velocity is less than 0.01 m/s and pressure is less then 5 Pa.

5.4.3 Discussion

Surface-tide velocities are 0.05 m/s along the slope and O(0.01 m/s) across the slope (Fig. 5.1b). Because topography just below the shelfbreak is super critical (i.e., $s/\alpha \geq 1$, where s is the topographic gradient, $\alpha = \sqrt{\omega^2 - f^2}/N$ the slope of a tidal characteristic, Fig. 5.1b), internal-tide rays generated at this location can propagate upward or downward. Where the bottom is super-critical, shoaling internal tides can be reflected to the deep ocean. Where the bottom is near-critical, shoaling internal tides can be critically reflected and turbulently dissipated (e.g., stations MP4 and X4.3, *Nash et al.*, 2007; *Martini et al.*, 2011a,b). Although topography does not exhibit a large-scale slope, Strong along-slope surface-tide velocities are expected to produce complicated three-dimensional internal tides over 1-3 km scale bumps.

Observed internal-tide velocities are elevated 500 m above the bottom near MP3 and MP5; and in the upper 1000 m across the slope (Fig. 5.3a). Generation-simulation velocities are smaller and elevated 500 m above the bottom at MP5 and near the bottom at L2.5, MP3, and X3.3 (Fig. 5.3b). Shoaling-simulation velocities are more comparable to the observations and are large within 500 m of the bottom and in the upper 1000 m (Fig. 5.3c). However, the shoaling simulation does not predict the large velocities observed 500 m above the bottom at MP3 and MP5. The phase of observed velocity bears little resemblance to that predicted by the generation simulation, but compares slightly better with the shoaling simulation (Fig. 5.3d-f). Both the observations and shoaling simulation indicate a 180° phase shift between the upper and lower halves of the water column.

Observed and simulated internal-tide pressures (Fig. 5.4) have less vertical structure than internal-tide velocities (Fig. 5.3). Observed pressure is predominantly low mode, but not mode-1; i.e., the upper-water pressure maximum occurs at 500 m depth rather than the

surface (Fig. 5.3a). Neither simulation predicts the observed amplitude of pressure (Fig. 5.3b-c). However, the simulations do predict the observed phase of bottom pressure (Fig. 5.3a-c), which determines internal-tide generation (*Kelly and Nash*, 2010). At the base of the slope, the observed phase of bottom pressure is consistent with both simulations, indicating the sign of observed internal-tide generation is predicted in the generation simulation. Near the shelfbreak, the phase of bottom pressure is consistent with the shoaling simulation, which is 180° different from the generation simulation. Therefore, near the shelfbreak, the sign of observed internal-tide generation will be opposite that predicted in the generation simulation.

By examining current ellipses, *Martini et al.* (2011a) concluded that the internal tide during this period was multidirectional. Our present comparison of the observations with two diagnostic simulations also suggests a superposition of locally-generated and shoaling wavefields. In particular, (i) the generation simulation, which is based upon realistic local forcing, does not predicted observed velocity and pressure, and (ii) the shoaling simulation, which roughly represents remote forcing, is consistent with the phase of observed pressure.

5.5   Energetics

Modal energy equations that include inter-modal energy conversion are used to quantify internal-tide generation and conversion to high modes on the Oregon continental slope.

5.5.1   Theory

Previous studies have derived surface and internal-tide energy equations by separating terms involving depth-averaged and residual quantities (e.g., *Kurapov et al.*, 2003; *Carter et al.*,

2008). These studies essentially extend a partial "flat-bottom" normal-mode decomposition over arbitrary topography. For instance, the surface tide, which is defined by depth-averages, is the 0th mode, and the internal tide, which is defined as residuals, is the sum of modes $n \geq 1$ (Appendix A). Here we complete this analogy by deriving energy equations for individual normal modes (see also *Llewellyn Smith and Young*, 2002; *Simmons et al.*, 2004; *Griffiths and Grimshaw*, 2007).

Tidally-averaged modal-energy equations are obtained by multiplying (5.1) by $\mathbf{u}_n^*$, multiplying the complex conjugate of (5.2) by p_n, adding both expressions, and depth integrating:

$$\frac{H}{2}\left[\hat{\mathbf{u}}_n^2 + \left(1 - \frac{f^2}{\omega^2}\right)\frac{\hat{p}_n^2}{c_n^2}\right]_t + \nabla \cdot (H\hat{\mathbf{u}}_n^*\hat{p}_n) = \sum_{m=0}^{\infty} C_n \ , \tag{5.4}$$

where c_n is the group velocity and hats indicate modal amplitudes (e.g., $p_n = \hat{p}_n\phi_n$, where ϕ_n is the vertical structure function). From left to right, the terms in (5.4) represent time change in energy, energy-flux divergence, and inter-modal energy conversion:

$$C_{m,n} = H\langle\mathbf{u}_m^* \cdot \nabla p_n - \mathbf{u}_n^* \cdot \nabla p_n\rangle \ , \tag{5.5}$$

which quantifies the rate of work done by mode m on mode n.

Internal-tide generation (e.g., *Niwa and Hibiya*, 2001; *Kurapov et al.*, 2003) is the rate of work done by the surface tide on the internal tide, and can be obtained from (5.5) by setting $m = 1$ and summing n from 1 to ∞:

$$C = \nabla H \cdot \mathbf{u}_0^* p'|_{z=H} \ . \tag{5.6}$$

In the deep ocean, where bottom drag is weak, internal-tide generation is a good proxy for surface-tide energy loss (*Jayne and St. Laurent*, 2001).

Because high mode tides are expected to dissipate quasi-locally (*St. Laurent and Garrett*, 2002; *Muller and Bühler*, 2009), the rate of work done on them may be a reasonable proxy for turbulent kinetic energy dissipation. For the purpose of this study, we define conversion to high modes as:

$$C_\epsilon = \sum_{m=0}^{2} \sum_{n=3}^{\infty} C_{m,n} \,, \tag{5.7}$$

where $n \geq 3$ are considered high modes.

An important property of (5.4), is that all terms are nonlinear, meaning the energetics of the generation and shoaling simulations cannot be linearly superimposed. The phasing of two wavefields determines thier covariance over a tidal cycle, which impacts energy, energy flux, and inter-modal energy conversion. *Kelly and Nash* (2010) recently highlighted the importance of phase in internal-tide generation. But, the effects of phasing are also important for energy conversion to higher modes.

5.5.2 Methods

We calculate normal modes and group velocities at each horizontal location by numerically solving the relevant eigenvalue problem (5.14) with a second-order finite difference matrix and horizontally-uniform $N^2(z)$ profile (e.g., *Smyth et al.*, 2010). To minimize the occurrence of spurious fits, the first twenty-five modal amplitudes of velocity and pressure are fit one-by-one using least-squares regression. Each fitted mode is removed before fitting the next. Only stations containing observations over 75% of the water column are decomposed into modes.

To remove dependence on $\nabla \hat{p}_n$, which is not measured, inter-modal conversion is

rewritten equivalently as the matrix:

$$C_{m,n} = H \langle \hat{\mathbf{u}}_m^* \phi_m \cdot \hat{p}_n \nabla \phi_n - \hat{\mathbf{u}}_n^* \phi_n \cdot \hat{p}_m \nabla \phi_m \rangle \ , \tag{5.8}$$

which only depends on spatial gradients of normal modes (which can be computed from topography and background stratification). In the analysis of observations and simulations, we calculate horizontal gradients of the normal modes using 2-km central differences in both horizontal directions.

5.5.3 Energy

Observed internal-tide energy (Fig. 5.5a and d) has an average across-slope magnitude of 1500 J/m^2, an order of magnitude smaller than observed at Kaena Ridge, Hawaii (*Nash et al.*, 2006), but similar to that observed 500 km from the Hawaiian Ridge (*Zhao et al.*, 2010). Internal-tide energy is greater than either numerical simulation (and more than double that of the generation simulation), further suggesting a superposition of locally-generated and shoaling internal tides.

High-mode tides are likely to dissipate locally because they propagate slowly and have large velocity shear (*St. Laurent and Garrett*, 2002). The observed internal tide contains more high-mode energy (i.e., modes 3-10) than the shoaling simulation, which in turn, contains more high-mode energy than the generation simulation. Therefore, we expect that the observed internal tide may dissipated more energy than either simulation. Additionally, we expect that shoaling internal tides will dissipate more energy than locally-generated internal tides. High-mode energy in the shoaling simulation is evidence of topographic scattering. For this simulation, the across-slope peak in high-mode energy occurs at

MP4, where the slope is predominantly near-critical. A similar peak is not found in the generation simulation, suggesting near-critical scattering is less important for dissipating locally-generated internal tides.

5.5.4 Energy Flux

Observed net internal-tide energy fluxes are approximately 500 W/m-coastline onshore (Fig. 5.6a and d), contrasting the generation simulation (500 W/m-coastline offshore, Fig. 5.6b and e), and complementing the shoaling simulation (500 W/m-coastline onshore, Fig. 5.6c and f). Because energy propagates at the group speed, which decreases with mode number, internal-tide energy flux is dominated by low modes.

While observed onshore energy flux indicates the presence of a shoaling internal tide, it does not preclude the simultaneous presence of a reflected or locally-generated offshore propagating internal tide. For instance, the generation simulation suggests their may be a 500 W/m-coastline offshore-propagating internal-tide, but this feature cannot be extracted from observed net energy-flux.

The observed decrease in energy flux with distance onshore indicates the Oregon slope is a sink of internal-tide energy. Unfortunately, the convergence of net energy flux alone does not determine whether internal-tide energy is scattered into along-slope propagating components, returned to the surface tide (*Kelly et al.*, 2010), or turbulently dissipated (*Kunze et al.*, 2002). However, locations of large energy-flux convergence (e.g., MP4, Fig. 5.5d) are associated with high-mode energy in the shoaling simulation (Fig. 5.5f), near-critical topography (Fig. 5.1b), and observed near-bottom turbulent bores (i.e., MP3 and MP4, *Martini et al.*, 2011b). Therefore, a portion of the energy-flux convergence is likely explained by turbulent dissipation.

5.5.5 Internal-Tide Generation

Surface-tide ellipses on the Oregon continental slope are oriented along large-scale isobaths (Fig. 5.1b); therefore, the generation simulation predicts most internal-tide generation over 1-3 km scale along-slope bumps (Fig. 5.7a). Much of the small-scale generation produces along-slope energy-flux divergences and convergences, which average-out over larger regions. Therefore, internal tides that are generated over across-slope topography and propagate offshore may be more important to the net energy balance. Offshore energy-flux in the generation simulation is about 500 W/m-coastline (Fig. 5.6a), consistent with the average surface-tide energy loss estimated by *Egbert and Ray* (2001) over a larger 80-km region. The shoaling simulation displays little internal-tide generation (Fig. 5.7c).

The across-slope integral of observed internal-tide generation at $43.2°$ N is 450 W/m-coastline, similar to that inferred from satellite observations over a larger region (*Egbert and Ray*, 2001). The across-slope structure of internal-tide generation indicates a maximum at X3.3, which is also present in the generation simulation (Fig. 5.7e). Observed generation at X5.7 is negative because the phase of bottom pressure is consistent with the shoaling simulation rather than the generation simulation. We interpret this as evidence that the shoaling internal tide modulates internal-tide generation (*Kelly and Nash*, 2010).

5.5.6 Energy Conversion to High Modes

Although C has been previously decomposed by mode (e.g., *Simmons et al.*, 2004; *Zilberman et al.*, 2009), and inter-modal energy conversion inferred from modal energy-flux divergences (*Johnston and Merrifield*, 2003), the analysis presented here may be the first to directly quantify energy conversion within the internal tide. Here we interpret energy conversion to

high modes, C_ϵ, as an imperfect proxy for turbulent kinetic energy dissipation. A benefit of C_ϵ is that it can be computed from sparse, large-scale, observations and pertains directly to cascade of tidal energy. A drawback of C_ϵ is that it may be positive or negative, unlike true energy dissipation, which is always positive.

In the generation simulation (Fig. 5.7b), C_ϵ has nearly equal regions of positive and negative values, indicating the local surface tide transfers little net energy to high modes. In the shoaling simulation (Fig. 5.7d), C_ϵ is positive over the lower portion of the slope, indicating the shoaling mode-1 tide is scattering to higher modes as it propagates onshore. These simulations suggest that shoaling internal tides on the Oregon slope dissipate energy more efficiently than locally generated internal tides.

At 43.2° N, C_ϵ is positive everywhere on the lower slope (except X3.3) and has an across-slope integral of 460 W/m-coastline. Similarly, observed C_ϵ (Fig. 5.7f) is maximized across the lower slope and has an across-slope integral of 470 W/m-coastline, consistent with the 500 W/m-coastline of observed turbulent kinetic energy dissipation (*Nash et al.*, 2007). *Martini et al.* (2011b) also associated the lower-slope (MP3 and MP4) with strong internal-tide shoaling and the generation of turbulent near-bottom bores.

5.6   Onshore and Offshore Energy Fluxes

In the study of multidirectional internal tides, there is no general (i.e., three-dimensional) method for resolving opposing and partially-offsetting energy fluxes. Here, we estimate onshore and offshore-propagating internal tides for each vertical mode by assuming along-slope uniformity. Some errors associated with this approximation are addressed in Appendix C.

5.6.1 Theory

In Appendix B, we show that tide-topography coupling can be confined to infinitely-thin topographic steps. Between topographic steps the bottom is flat and $\hat{u}_n$ and $\hat{p}_n$ can be written:

$$\hat{u}_n = A_n e^{ik_n x} + B_n e^{-ik_n x} \tag{5.9}$$

$$\hat{p}_n = c_n A_n e^{ik_n x} - c_n B_n e^{-ik_n x} \ , \tag{5.10}$$

where A_n and B_n are complex amplitudes of harmonic fits that represent onshore and offshore-propagating waves. $\hat{p}_n$ has been solved from $\hat{u}_n$ by modally-decomposing (5.1) and using the relation $c_n = \omega/k_n(1 - f^2/\omega^2)$. Transverse velocity, v_n is non-zero because of planetary rotation, but also varies sinusoidally in x.

Replacing $\hat{u}_n$ and $\hat{p}_n$ with wave amplitudes, the two-dimensional tidally-averaged energy equation (over the locally-flat bottom) becomes:

$$H \left(A_n^2 + B_n^2\right)_t + \left(Hc_n A_n^2 - Hc_n B_n^2\right)_x = 0 \ . \tag{5.11}$$

Internal-tide energy flux may be arbitrarily small when A_n and B_n have similar magnitudes (i.e., form a standing wave). Therefore, weak internal-tide energy flux is not uniquely associated with weak internal-tide energy. Although energy flux in the direction transverse to wave propagation is non-zero, it does not have a physical interpretation because it is non-divergent and does not appear in the energy budget.

5.6.2 Methods

Tidally-averaged energies (but not phases) of onshore and offshore-propagating internal tides are obtained for each mode by inverting (5.9) and (5.10):

$$A_n^2 = \frac{1}{4}|\hat{u}_n + \hat{p}_n/c_n|^2 \qquad (5.12)$$

$$B_n^2 = \frac{1}{4}|\hat{u}_n - \hat{p}_n/c_n|^2 \; . \qquad (5.13)$$

5.6.3 Discussion

Separating observations into onshore and offshore-propagating internal tides indicates that approximately 1000 W/m-coastline is shoaling and 500 W/m-coastline is radiating offshore (Fig. 5.8a, d, and g). The generation simulation roughly predicts the observed peaks in offshore energy flux near regions of strong internal-tide generation (e.g., near X3.3 and X5.3, Fig. 5.8b, e, and h). The shoaling simulation predicts the decrease in onshore energy flux with distance onshore (Fig. 5.8c, f, and i). A lack of offshore energy flux in this simulation indicates that the shoaling internal tide is scattered/dissipated rather than reflected.

The shoaling internal tide appears to supply 1000 W/m-coastline to the Oregon slope, roughly twice the observed turbulent kinetic energy dissipation (*Nash et al.*, 2007). We propose that 3-D effects, such as along-slope energy-flux divergence, explain the excess energy-flux convergence. Unfortunately, these dynamics are difficult to assess without (i) observations of along-slope variability and (ii) knowledge of the true shoaling tide. However, both simulations contain along-slope energy-flux divergences that have amplitude O(500 W/m-coastline).

5.7   Conclusions

The Oregon continental slope is home to locally-generated and shoaling internal tides that interact vigorously with topography. We have illuminated these processes using a new theory of linear tide-topography coupling (Section 5.5). Direct observations indicate the surface tide scatters 450 W/m-coastline to the internal tide, which approximately equals satellite-derived surface-tide energy loss (*Egbert and Ray*, 2001). In addition, surface and low-mode internal tides scatter 470 W/m-coastline to high-mode internal tides, which approximately equals observed turbulent kinetic-energy dissipation (*Nash et al.*, 2007). Lastly, we have estimated onshore and offshore energy fluxes, but are unable to close the energy budge without considering 3-D dynamics.

Although the results presented here are specific to the Oregon slope, the importance of linear tide-topography coupling likely pertains to continental margins as a whole. These features provide a large surface area to catch and scatter shoaling internal tides. Like previous investigations, we have found evidence that shoaling internal tides are not elastically reflected (*Alford and Zhao*, 2007), but instead scattered to higher modes and dissipated quasi-locally (*Nash et al.*, 2004).

5.8   Appendix A: Normal Modes

Without loss of generality, the depth-structure of pressure and velocity can be isolated in a set of functions, $\phi_n(z)$, reducing (5.1) and (5.2) to an eigenvalue problem at *each* horizontal location:

$$\left(\frac{\phi_{nz}}{N^2}\right)_z + \left(1 - \frac{f^2}{\omega^2}\right)\frac{\phi_n}{c_n^2} = 0 , \tag{5.14}$$

where ϕ_n and c_n^2 are eigenfunctions and eigenvalues, respectively. The eigenfunctions are orthonormal:

$$\langle \phi_m \phi_n \rangle = \delta_{m,n} \tag{5.15}$$

and complete, so that projections of pressure and velocity onto this basis are uniformly convergent (i.e., variance conserving) even when ϕ_n do not obey local boundary conditions:

$$(\mathbf{u}, \ p) = \sum_{n=0}^{\infty} (\mathbf{u}_n, \ p_n) \ , \tag{5.16}$$

where $\mathbf{u}_n = \hat{\mathbf{u}}(\mathbf{x})\phi_n(z)$ and $p_n = \hat{p}(\mathbf{x})\phi_n(z)$. To connect our analysis to an extensive body of existing literature, ϕ_n are chosen to obey a rigid-lid ($\phi_{nz} = 0$ at $z = 0$) and flat bottom ($\phi_{nz} = 0$ at $z = H$) (e.g., *Gill*, 1982).

Although a normal-mode decomposition does not always converge point-wise at the bottom boundary, it always conserves energy, regardless of the topographic slope. Using normal modes to decompose flow over sloping topography produces effects that are analogous to Fourier transforming a finite-length timeseries with an endpoint mismatch. The Fourier Transform conserves energy, but the mismatch causes leakage and redistributes energy into a characteristic f^{-2} shape. In regions of sloping topography, we expect internal-tide energy to exhibit an analogous n^{-2} shape.

5.9   Appendix B: A Topographic Step

Here, we show that decomposing tidal flow with normal modes is equivalent to approximating topography as piecewise-constant. Consider a tidally-averaged internal tide

in steady-state: at any topographic step, inter-modal energy conversion must equal energy-flux divergence:

$$C_n = \left\langle H^+ u_n^{*+} p_n^+ - H^- u_n^{*-} p_n^- \right\rangle / \delta x \; , \tag{5.17}$$

where δx is an arbitrarily small distance and superscripts denote variables on the left $(^-)$ and right $(^+)$ sides of the step. Transverse velocity may be nonzero due to planetary rotation but produces no energy-flux divergence.

We match the solutions at the step by requiring volume conservation and continuous pressure:

$$H^- u^- = H^+ u^+ \tag{5.18}$$

$$p^- = p^+ \; . \tag{5.19}$$

Using the orthogonality condition (5.15) these conditions are substituted in (5.17) to produce:

$$C_n = \left\langle H^- u^{*-} p_n^+ - H^- u_n^{*-} p^+ \right\rangle / \delta x \; . \tag{5.20}$$

Adding and subtracting $H^- u_n^{*-} p_n^-$ (and invoking the orthogonality condition) results in:

$$C_n = H^- \left\langle u^{*-} \frac{p_n^+ - p_n^-}{\delta x} - u_n^{*-} \frac{p^+ - p^-}{\delta x} \right\rangle \; , \tag{5.21}$$

which reduces to the general expression for inter-modal energy conversion (5.5) (summed over all m) as $\delta x \to 0$. Physically, this derivation confirms that flat-bottom dynamics such as modal wave-speeds are descriptive everywhere and conceptually all tide-topography coupling is confined to infinitely-thin topographic steps.

5.10   Appendix C: Sensitivity of the 2-D Approximation

We conduct two sensitivity experiments to examine errors associated with assuming that internal tides are propagating in the across-slope plane. The first experiment considers only a single-mode, 500 W/m-coastline, offshore-propagating internal tide (Fig. 5.9a). The direction of the tide's propagation is varied between $\theta \pm 90°$ from due west. As the angle deviates from zero, actual offshore energy flux decreases proportional to $\cos\theta$. Estimated onshore and offshore energy fluxes are computed from (5.12) and (5.13). We find the two-dimensional approximation predicts actual offshore energy flux within 20% provided $|\theta| < 60°$.

The second experiment considers a single-mode, 1000 W/m-coastline, onshore-propagating tide is superimposed on a single-mode, 500 W/m-coastline, offshore-propagating tide (Fig. 5.9b). The direction of the offshore-propagating tide is fixed (as due west), but the direction of the onshore-propagating tide is varied between $\theta \pm 90°$ from due east, which affects estimates of offshore energy flux. Additionally, the phase difference between the onshore and offshore-propagating tides also affects the accuracy of the two-dimensional approximation. The worst possible phase restricts accurate energy-flux estimates to situations where $|\theta| < 15°$. However, the median phase allows energy-flux estimates for $|\theta| < 50°$. These sensitivity experiments suggest that estimated onshore and offshore energy fluxes are generally within 20% of the true values, even when internal tides are propagating at at $|\theta| \approx 50°$ to the across-slope plane.

5.11 Appendix D: Verifying the Modal Decomposition

The accuracy of the modal-energy equations (5.4) is most easily (and accurately) assessed in a fluid with constant stratification (i.e., constant N^2). In such a flow the vertical structure functions have a simple analytical form:

$$\phi_n = \sqrt{2} \cos \left[\frac{n\pi}{H} (z + H) \right] \quad \text{for} \quad n > 0 . \tag{5.22}$$

Modal fits are obtained by simply extending u and p to positive z by even reflection and decomposing the profile using a Fast Fourier Transform. Here we analyze the BT and BC sims. described in Chapter 4. The modal decompositions of velocity and pressure are shown in Fig. 5.10. Velocities are similar in both simulations and contain both low and high-mode variability. Pressures differ between simulations, but contain mostly low-mode variability.

When flow has reached an approximate steady-state, the tidally-averaged modal-energy equations reduce to:

$$\nabla \cdot \langle H \mathbf{u}_n^* p_n \rangle = C_n , \tag{5.23}$$

where the analytical form of ϕ_n simplifies C_n to:

$$C_n = \nabla H \cdot \sum_{n=0}^{\infty} \left(\frac{n^2}{n^2 - m^2} \hat{\mathbf{u}}_m^* \, \hat{p}_n - \frac{m^2}{m^2 - n^2} \hat{\mathbf{u}}_n^* \, \hat{p}_m \right) . \tag{5.24}$$

By evaluating these terms in the simulations, the modal-energy balances are shown to be accurate for several modes (Fig. 5.11).
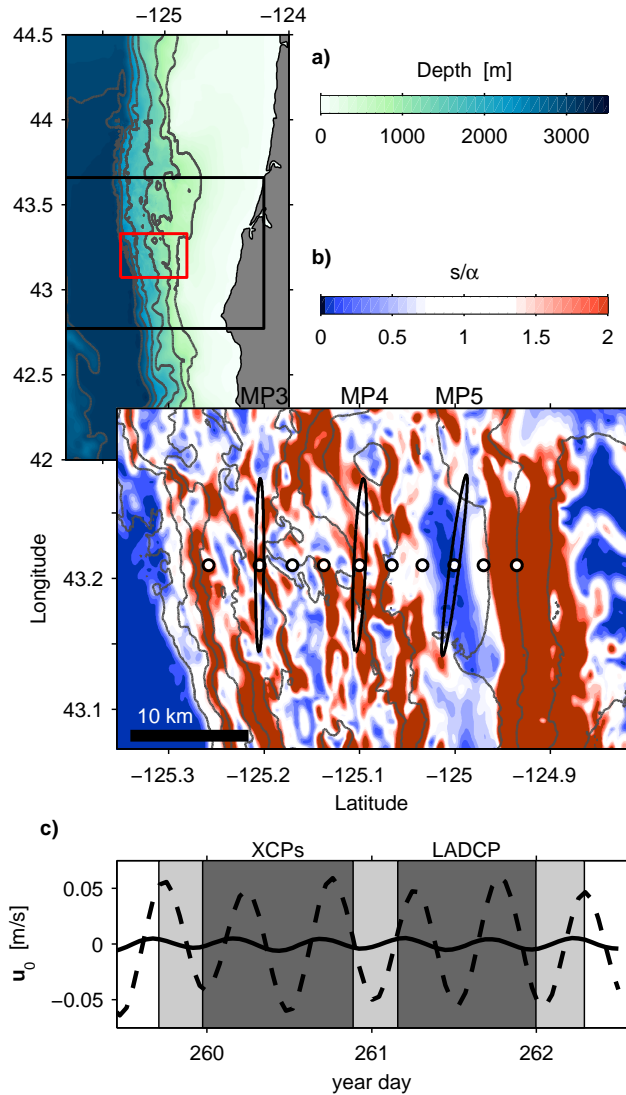
Acknowledgments

Figure 5.1: Oregon-slope topography and surface tide. (a) Large-scale topography (contours every 500 m). The model domain is outlined in black and the location of observational study in red. (b), Local east-west topographic gradient normalized by the slope of a semidiurnal tidal ray (contour are every 250 m). Dots indicate location of observations and ellipses represent tidal excursions amplified by 10. (c), Timeseries of across-slope (solid) and along-slope (dashed) surface-tide velocities during XCP and LADCP measurements (dark gray) and sub-sampled MP measurments (light gray).
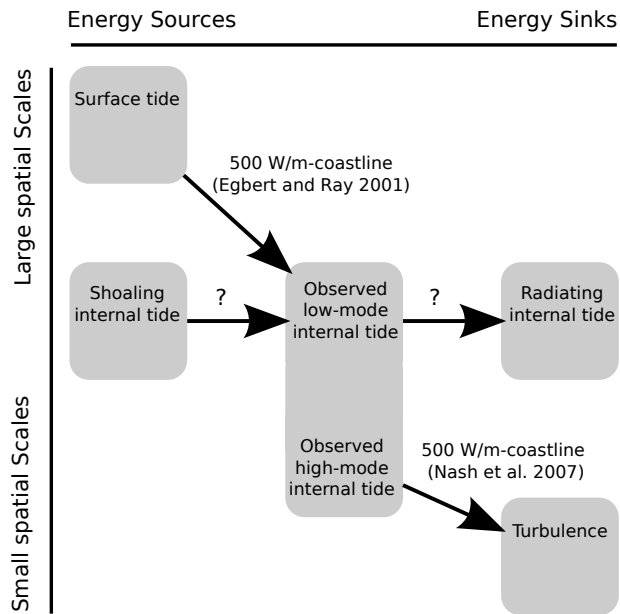
Figure 5.2: Schematic of tidal energetics on the Oregon slope. Surface tides and shoaling internal tides supply energy to the local internal tide, which partially radiates and partially dissipates. Our goals are to quantify the amplitudes of shoaling and radiating internal tides and to determine if tide-topography coupling explains surface-tide energy loss and local turbulence.
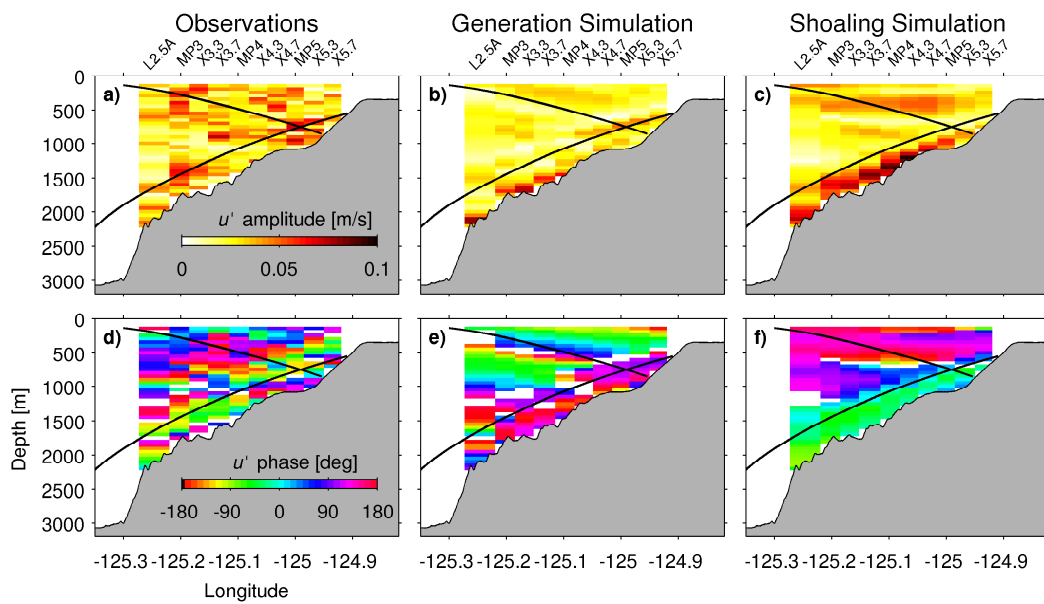
Figure 5.3: Amplitudes (a-c) and phases (d-f) of internal-tide velocity. From left to right columns contain observations, the generation simulation, and the shoaling simulation. Black lines indicate example tidal characteristics.
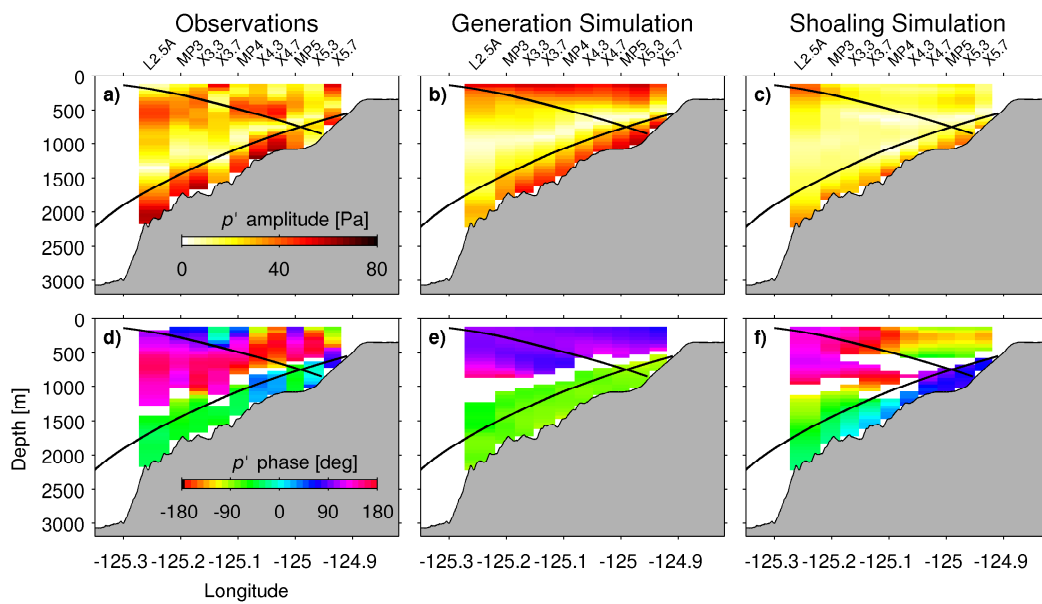
Figure 5.4: Amplitudes (a-c) and phases (d-f) of internal-tide pressure. From left to right columns contain observations, the generation simulation, and the shoaling simulation. Black lines indicate example tidal characteristics.
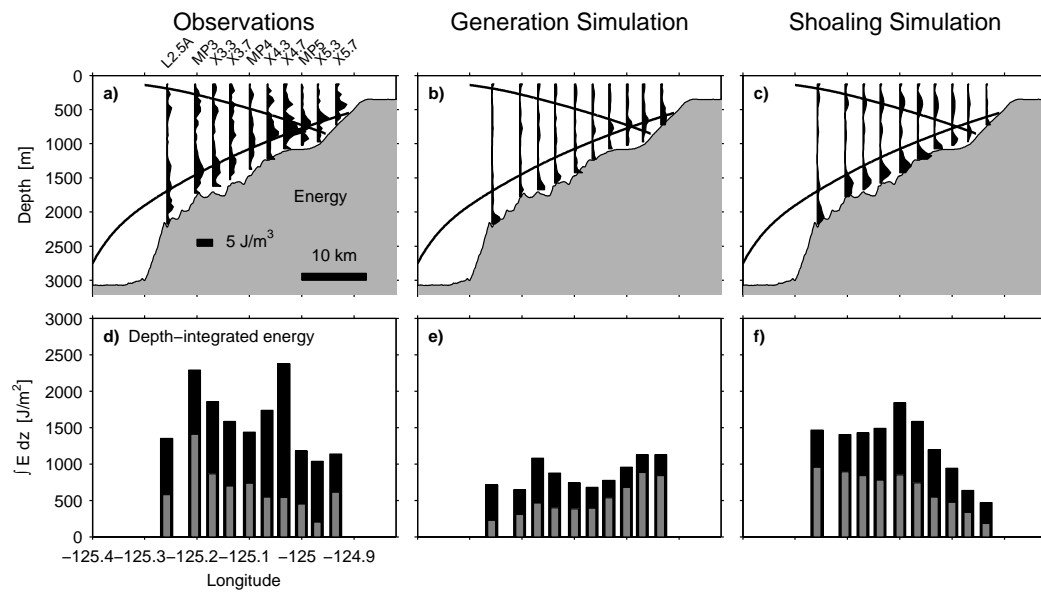
Figure 5.5: Depth-structure (a-c) and depth-integrals (d-f) of internal-tide energy. From left to right columns contain observations, the generation simulation, and the shoaling simulation. Gray integrals indicate contributions by modes 1 and 2.
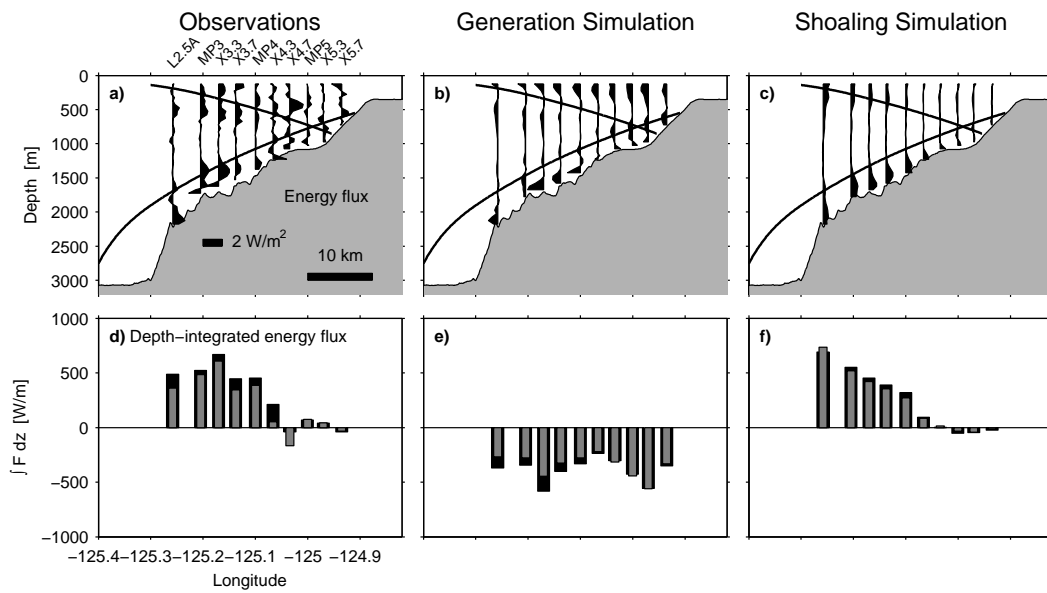
Figure 5.6: Depth-structure (a-c) and depth-integrals (d-f) of internal-tide energy flux. From left to right columns contain observations, the generation simulation, and the shoaling simulation. Gray integrals indicate contributions by modes 1 and 2.
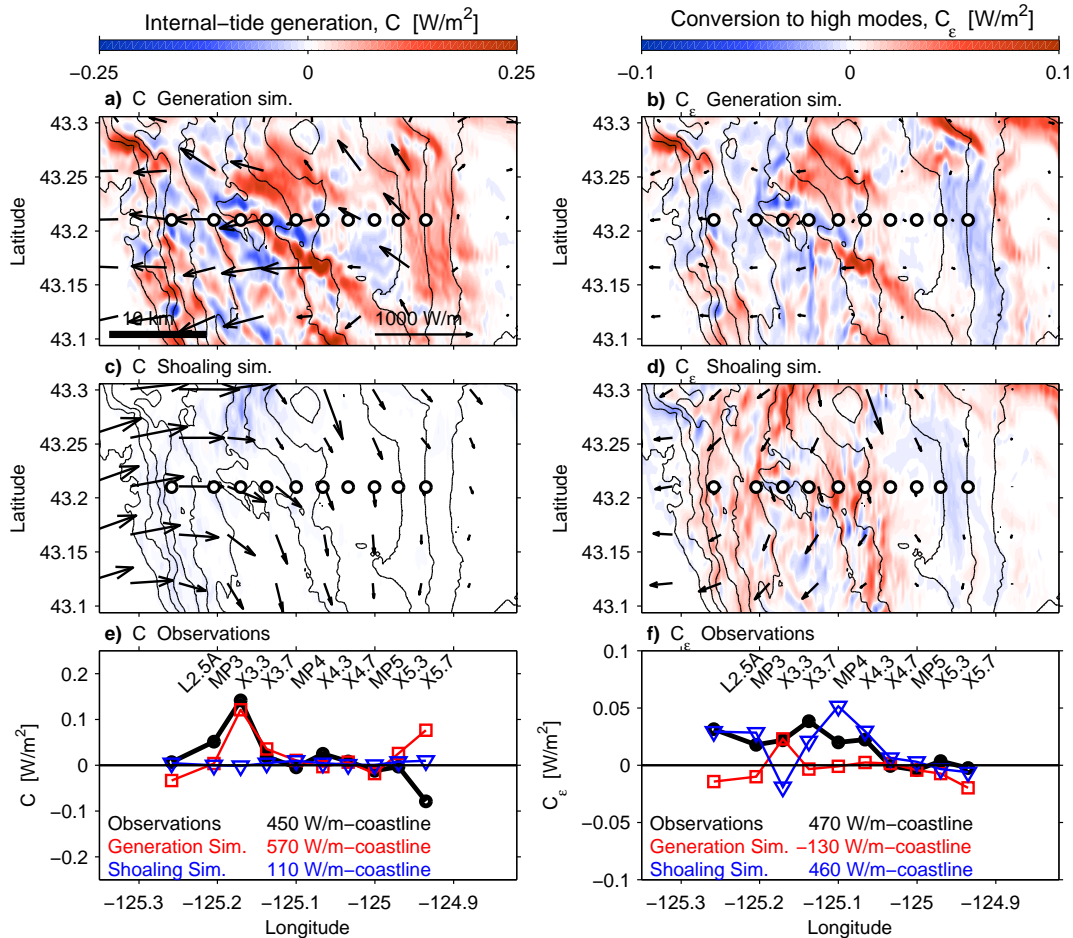
Figure 5.7: Spatial maps of inter-modal energy conversion. (a) and (c), internal-tide generation in the generation and shoaling simulations, respectively. Arrows indicate internal-tide energy fluxes. (b) and (d) energy conversion to high modes ($n \geq 3$) in the generation and shoaling simulations, respectively. Arrows indicate high-mode energy fluxes. (e) and (f), observed and simulated internal-tide generation and energy conversion to high modes, respectively, at $43.2°$ N.

Figure 5.8: Onshore and offshore-propagating internal tides. From left to right, columns contain observations, the generation simula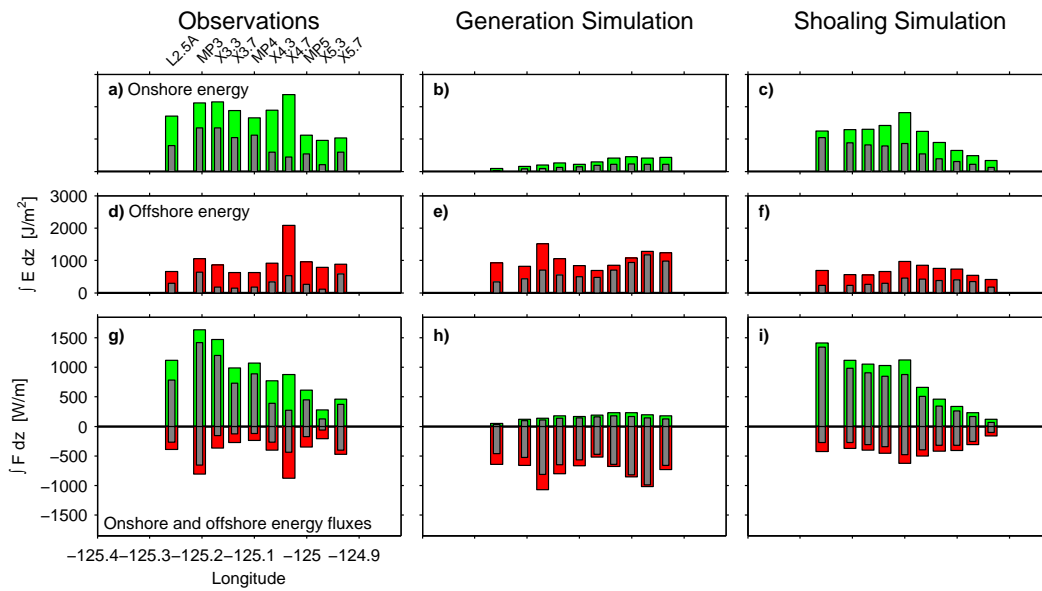tion, and the shoaling simulation. Depth-integrated energy associated with onshore (a-c) and offshore-propagating (d-f) internal tides. Depth-integrated energy flux (g-i) associated with onshore- and offshore-propagating internal tides. In all graphs, gray indicates contributions by modes 1 and 2.
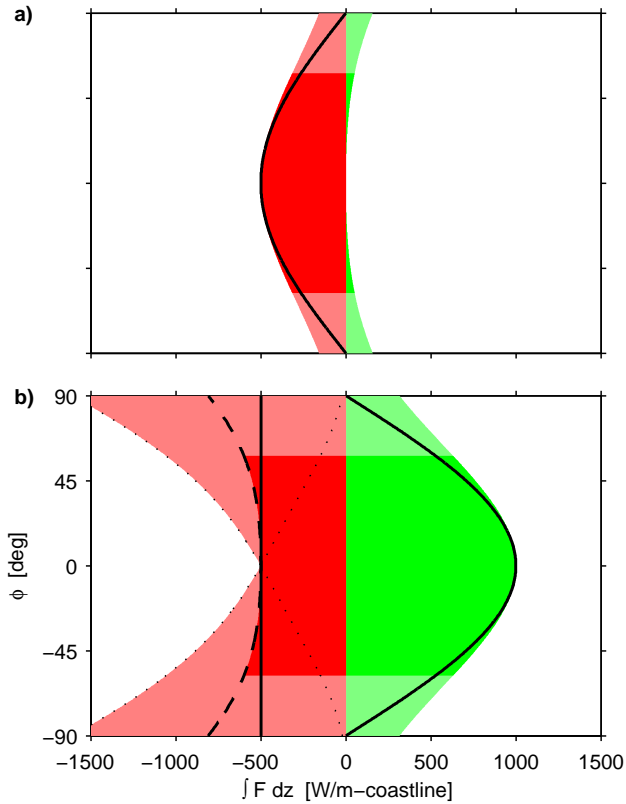
Figure 5.9: Sensitivity of the two-dimensional approximation. In both (a) and (b) thick black lines indicate true onshore and offshore energy fluxes. Green and red regions indicate estimated onshore and offshore energy fluxes. Dark green and red indicate regions where estimated energy flux is with 20% of true energy flux. In (a) the propagation angle of a 500 W/m-coastline tide is varied between $\theta \pm 90°$ from due west. In (b) a 500 W/m-coastline tide propagates due west while the propagation angle of a 1000 W/m-coastline tide is varied between $\theta \pm 90°$ from due east. The phase difference between the onshore and offshore-propagating tides affects the estimated fluxes, the median estimate is denoted by a dashed line and best and worst-case scenarios are denoted by thin black lines.
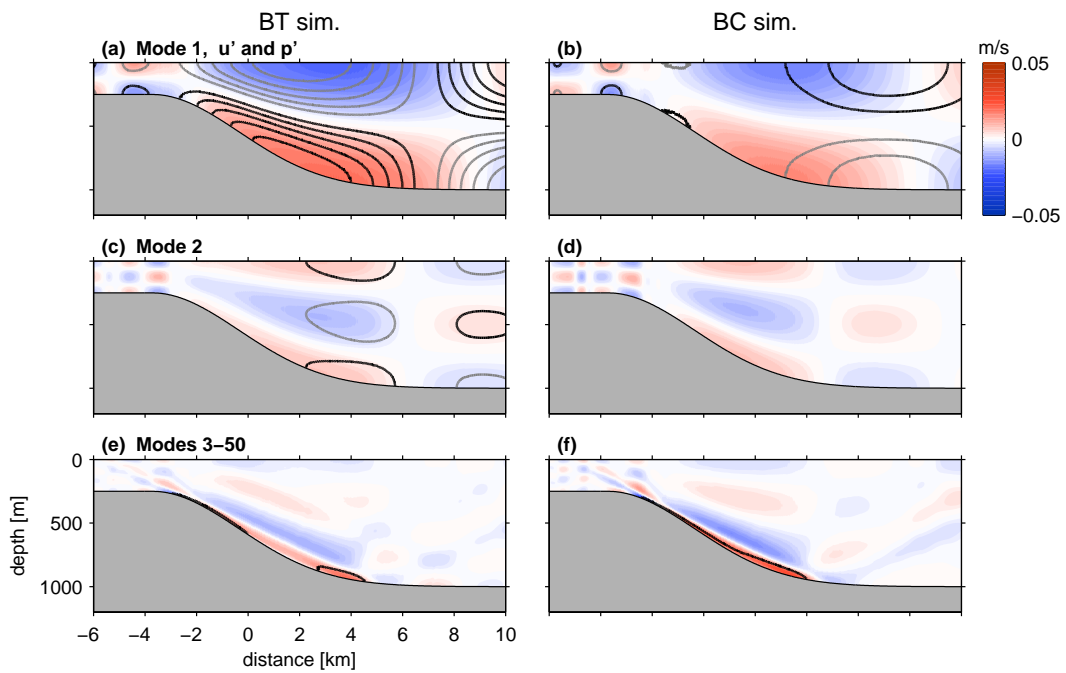
Figure 5.10: Internal-tide velocity (color) and pressure (contour) by normal mode. Pressure contours are every 5 Pa; black contours are positive, gray contours are negative. Left column: modes 1 (a), 2 (c), and 3-50 (e) from the BT sim. Right column: modes 1 (b), 2 (d), and 3-50 (f) from the BC sim.
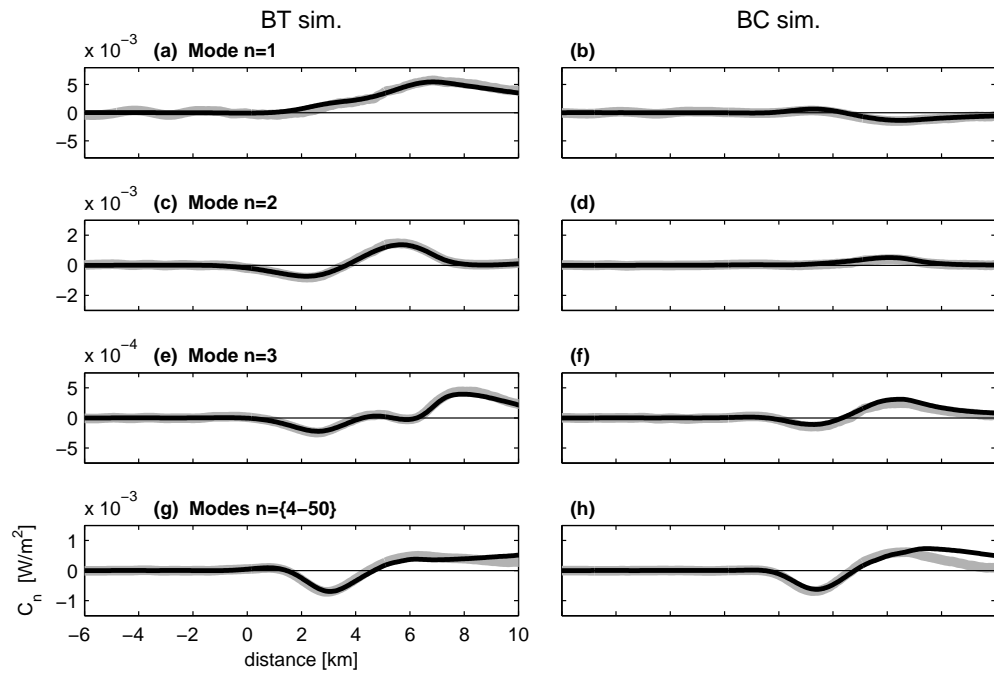
Figure 5.11: Internal-tide energy balances by mode. For each mode, energy conversion C_n (black) balances energy flux divergence $\nabla \cdot F_n$ (gray). Left column: modes 1 (a), 2 (c), 3 (e), and 4-50 (g) from the BT sim. Right column: modes 1 (b), 2 (d), 3 (f), and 4-50 (h) from the BC sim.

6. CONCLUSIONS

"There is a good chance that the whole question concerning the present tidal dissipation can be tied down in the next five years" -Walter Munk (1968)

Three hundred years after Newton explained the source of tides, we are still learning about their demise. In the previous chapters we have investigated the origin, variability, and cascade of internal-tide energy. An underlying theme has been the rich dynamics of linear tide-topography coupling. Over the last decade, the general expression for linear internal-tide generation over arbitrary topography has emerged (Chapter 2):

$$C = \nabla H \cdot \overline{\mathbf{U}p'}|_{z=H} . \tag{6.1}$$

This expression implies the relevance of a normal-mode decomposition over topography and results in unambiguous internal-tide pressures and well-defined depth-profiles of internal-tide energy flux (Chapters 2 and 3).

Analyzing the mathematical form of C will likely produce new analytical approximations for internal-tide generation and better define relevant topographic scales for internal-tide generation. In Chapter 4 this expression revealed the roles of preexisting internal tides in internal-tide generation, which partially explains their intermittency and indicates that they may resonate across ocean basins.

Applying a complete normal-mode decomposition to the tidal-energy budget produces

an expression for modal-energy conversion (Chapter 5):

$$C_{m,n} = H \left\langle \overline{\mathbf{u}_m \cdot \nabla p_n - \mathbf{u}_n \cdot \nabla p_m} \right\rangle \;, \tag{6.2}$$

which concisely describes interactions between normal modes as they encounter sloping topography.

Quantifying tide-topography coupling $C_{m,n}$ from observations on the Oregon continental shelf has identified multiple sources for internal-tide energy (Chapter 5). These sources suggest that internal tides are locally generated and radiated to the deep ocean, while at the same time, shoaling internal tides scatter on the slope and drive turbulent mixing. These observations support the view that tidal-energy dissipation occurs where internal tides shoal, reinforcing the notion that spatial distributions of internal-tide dissipation and generation are unique.

In mapping the global distribution of internal-tide dissipation, we may be able to rely on the linear formulas, such as $C_{m,n}$, which are designed to describe large-scale low-mode internal-tide scattering. This is because once low-mode internal tides scatter into higher modes, they propagate slowly and are unlikely to travel far before dissipating, regardless of how the dissipation occurs. With the continued analysis of satellite observations and global numerical models, we will hopefully soon be able to estimate internal-tide dissipation via low-mode scattering.

In Chapter 5, it was shown that separating onshore and offshore-propagating internal tides can remove interference patterns that result in non-descriptive energy fluxes (*Nash et al.*, 2004; *Martini et al.*, 2007). Interference patterns, as illustrated by *Rainville et al.* (2010) and *Zhao et al.* (2010), remain a hurdle to tracking individual internal tides from generation to dissipation. Decomposing internal tides into normal modes simplifies the

discussion of interference to a series of two-dimensional maps, which are only coupled over sloping topography. A daunting (perhaps impossible) task is to invert these interference patterns to obtain the individual component internal-tides. Such a wave description of global internal tides would be useful and remains a task for future investigators.

Bibliography

Alford, M. H. (2003), Redistribution of energy available for ocean mixing by long-range propagation of internal waves, *Nature*, *423*, 159–162, doi:10.1038.

Alford, M. H., and Z. Zhao (2007), Global patterns of low-mode internal-wave propagation. Part II: group velocity, *J. Phys. Oceanogr.*, *37*, 1849–1858.

Alford, M. H., M. C. Gregg, and M. A. Merrifield (2006), Structure, propagation and mixing of energetic baroclinic tides in Mamala Bay, Oahu Hawaii, *J. Phys. Oceanogr.*, *36*, 997–1018.

Alford, M. H., J. A. MacKinnon, Z. Zhao, R. Pinkel, J. Klymak, and T. Peacock (2007), Internal waves across the pacific, *Geophys. Res. Lett.*, *34*, L24,601, doi:10.1029/2007GL031,566.

Althaus, A. M., E. Kunze, and T. B. Sanford (2003), Internal tide radiation from Mendocino Escarpment, *J. Phys. Oceanogr.*, *33*, 1510–1527.

Arbic, B. K., A. J. Wallcraft, and E. J. Metzger (2010), Concurrent simulation of the eddying general circulation and tides in a global ocean model, *Ocean Modelling*, *32*, 175–187.

Baines, P. G. (1973), The generation of internal tides by flat-bump topography, *Deep-Sea Res.*, *20*, 179–205.

Baines, P. G. (1974), The generation of internal tides over steep continental slopes, *Philos. Trans. R. Soc. Lond.*, *A277*, 27–58.

Baines, P. G. (1982), On internal tide generation models, *Deep-Sea Res.*, *29*, 307–338.

Bell, T. H. (1975a), Lee waves in stratified flows with simple harmonic time dependence, *J. Fluid Mech.*, *64*, 705–722.

Bell, T. H. (1975b), Topgraphically generated internal waves in the open ocean, *J. Geophys. Res.*, *80*, 320–327.

Butman, B., P. S. Alexander, A. Scotti, R. C. Beardsley, and S. P. Anderson (2006), Large internal waves in Massachusetts Bay transport sediments offshore, *Cont. Shelf Res.*, *26*, 2029–2049.

Cacchione, D. A., L. F. Pratson, and A. S. Ogston (2002), The shaping of the continental slopes by internal tides, *Science*, *296*, 724–727.

Carter, G. S., M. C. Gregg, and M. A. Merrifield (2006), Flow and mixing around a small seamount on Kaena Ridge, Hawaii, *J. Phys. Oceanogr.*, *36*, 1036–1052.

Carter, G. S., M. A. Merrifield, J. M. Becker, K. Katsumata, M. C. Gregg, D. S. Luther, M. D. Levine, T. J. Boyd, and Y. L. Firing (2008), Energetics of M_2 barotropic-to-baroclinic tidal conversion at the Hawaiian Islands, *J. Phys. Oceanogr.*, *38*, 2205–2223.

Cartwright, D. E. (1999), *Tides: A Scientific history*, Cambridge University Press.

Chuang, W., and D. P. Wang (1981), Effects of a density front on the generation and propagation of internal tides, *J. Phys. Oceanogr.*, *11*, 967–996.

Colosi, J. A., and W. Munk (2006), Tales of the venerable Honolulu tide gauge, *J. Phys. Oceanogr.*, *36*, 967–996.

Cox, C. S., and H. Sandstrom (1962), Coupling of internal and surface waves in water of variable depth, *J. Oceanog. Soc. Japan*, *20*, 499–513.

Craig, P. D. (1987), Solutions for internal tide generation over coastal topography, *J. Mar. Res.*, *45*, 83–105.

Cummins, P. F., and L. Y. Oey (1997), Simulation of barotropic and baroclinic tides off Northern British Columbia, *J. Phys. Oceanogr.*, *27*, 762–781.

D'Asaro, E. (1985), The energy flux from the wind to near-inertial motions in the surface mixed layer, *J. Phys. Oceanogr.*, *15*, 1043–1059.

Desaubies, Y., and M. C. Gregg (1981), Reversible and irreversible finestructure, *J. Phys. Oceanogr.*, *11*, 541–556.

Di Lorenzo, E., W. R. Young, and S. Llewellyn Smith (2006), Numerical and analytical estimates of M_2 tidal conversion at steep oceanic ridges, *J. Phys. Oceanogr.*, *36*, 1072–1084.

Duda, T. F., and L. Rainville (2008), Diurnal and semidiurnal internal tide energy flux at a continental slope in the South China Sea, *J. Geophys. Res.*, *113*, C03,025, doi:10.1029/2007JC004,418.

Dushaw, B. D. (2006), Mode-1 internal tides in the western North Atlantic Ocean, *Deep Sea Res. I*, *53*, 449–473.

Dushaw, B. D., and P. F. Worcester (1998), Resonant diurnal internal tides in the North Atlantic, *Geophys. Res. Lett.*, *25*, 2189–2192.

Echeverri, P., and T. Peacock (2010), Internal tide generation by arbitrary two-dimensional topography, *J. Fluid Mech.*, *649*, 247–266.

Egbert, G. D. (1997), Tidal data inversion: Interpolation and inference, *Prog. in Oceanogr.*, *40*, 81–108.

Egbert, G. D., and R. D. Ray (2000), Significant dissipation of tidal energy in the deep ocean inferred from satellite altimeter data, *Nature*, *405*, 775–778.

Egbert, G. D., and R. D. Ray (2001), Estimates of M2 tidal energy dissipation from TOPEX/POSEIDON altimeter data, *J. Geophys. Res.*, *106*, 22,475–22,502.

Eriksen, C. C. (1998), Internal wave reflection and mixing at Fieberling Guyot, *J. Geophys. Res.*, *103*, (C2) 2977–2994.

Garrett, C., and E. Kunze (2007), Internal tide generation in the deep ocean, *Annu. Rev. Fluid Mech.*, *39*, 57–87.

Gayen, B., and S. Sarkar (2010), Turbulence during the generation of internal tide on a critical slope, *Phys. Rev. Lett.*, *104*, 218,502.

Gerkema, T., and H. van Haren (2007), Internal tides and energy fluxes over Great Meteor Seamount, *Ocean Sci.*, *3*, 441–449.

Gerkema, T., F. A. Lam, and L. R. M. Maas (2004), Internal tides in the Bay of Biscay: conversion rates and seasonal effects, *Deep-Sea Res.*, *51*, 2995–3008.

Gerkema, T., C. Staquet, and P. Bouruet-Aubertot (2006), Non-linear effects in internal-tide beams, and mixing, *Ocean Modelling*, *12*, 302–318.

Gilbert, D., and C. Garrett (1989), Implications for ocean mixing of internal wave scattering off irregular topography, *J. Phys. Oceanogr.*, *19*, 17161729.

Gill, A. E. (1982), *Atmosphere-ocean dynamics*, Academic Press.

Griffiths, S. D., and R. H. J. Grimshaw (2007), Internal tide generation at the continental shelf modeled using a modal decomposition: two-dimensional results, *J. Phys. Oceanogr.*, *37*, 428–451.

Helland-Hansen, B., and F. Nansen (1909), The Norwegian Sea: Its physical oceanogrpahy based upon the Norwegian researches 1900-1904, *Report on Norwegian Fishery and Marine-invsetications*, *11*.

Hendershott, M. C. (1981), Long waves and ocean tides, in *Evolution of physical oceanography: Scientific Surveys in honor of Henry Stommel*, edited by B. A. Warren and C. Wunsch, pp. 292–341, The MIT Press.

Holloway, P. E. (1996), A numerical model of internal tides with application to the Australian North West Shelf, *J. Phys. Oceanogr.*, *26*, 21–37.

Jayne, S. R., and L. C. St. Laurent (2001), Parameterizing tidal dissipation over rough topography, *Geophys. Res. Lett.*, *28*, 811–814.

Jeffreys, H. (1920), Tidal friction in shallow seas, *Phil. Trans. Roy. Soc.*, *221*, 239–264.

Jeffreys, H. (1926), On fluid motions produced by differences of temperature and humidity, *Q. J. Roy. Meteor. Soc.*, *51*, 347356.

Johnston, T. M. S., and M. A. Merrifield (2003), Internal tide scattering at seamounts, ridges, and islands, *J. Geophys. Res.*, *108 (C6)*, 3180, doi:10.1029/2002JC001,528.

Johnston, T. M. S., M. A. Merrifield, and P. E. Holloway (2003), Internal tide scattering at the Line Islands Ridge, *J. Geophys. Res.*, *108 (C11)*, 3365, doi:10.1029/2003JC001,844.

Kelly, S. M., and J. D. Nash (2010), Internal-tide generation and destruction by shoaling internal tides, *Geophys. Res. Lett.*, accepted.

Kelly, S. M., J. D. Nash, and E. Kunze (2010), Internal-tide energy over topography, *J. Geophys. Res.*, p. doi:10.1029/2009JC005618.

Khatiwala, S. (2003), Generation of internal tides in an ocean of finite depth: analytical and numerical calculations, *Deep-Sea Res.*, *50*, 3–21.

Kundu, P. K., and I. M. Cohen (2002), *Fluid Mechanics*, Academic Press.

Kunze, E., L. K. Rosenfeld, G. S. Carter, and M. C. Gregg (2002), Internal waves in Monterey Submarine Canyon, *J. Phys. Oceanogr.*, *32*, 1890–1913.

Kurapov, A., G. Egbert, J. S. Allen, R. N. Miller, S. Y. Erofeeva, and P. M. Kosro (2003), The M_2 internal tide off Oregon: Inferences from data assimilation, *J. Phys. Oceanogr.*, *33*, 1733–1757.

Legg, S., and K. M. H. Huijts (2006), Preliminary simulations of internal waves and mixing generated by finite amplitude tidal flow over isolated topography, *Deep-Sea Res.*, *53*, 140–156.

Lerczak, J., C. Winant, and M. Hendershott (2003), Observations of the semidiurnal internal tide on the southern California slope and shelf, *J. Geophys. Res*, *108*, C33,068, doi:10.1029/2001JC001,128.

Llewellyn Smith, S. G., and W. R. Young (2002), Conversion of the barotropic tide, *J. Phys. Oceanogr.*, *32*, 1554–1566.

Lu, Y., D. G. Wright, and D. Brickman (2001), Internal tide generation over topography: experiments with a free-surface z-level ocean model, *J. of Atmos. and Ocean. Tech.*, *18*, 1076–1091.

Maas, L. R. M., D. Benielli, J. Sommeria, and F. P. A. Lam (1997), Observation of an internal wave attractor in a confined, stably stratified fluid, *Nature*, *388*, 557–561.

MacKinnon, J. A., and K. B. Winters (2005), Subtropical catastrophe: Significant loss of low-mode tidal energy at 28.9, *Geophys. Res. Lett.*, *32*, L15,605.

Manders, A. M. M., L. R. M. Maas, and T. Gerkema (2004), Observations of internal tides in the Mozambique Channel, *J. Geophys. Res.*, *109*, C12,034, doi:10.1029/2003JC002,187.

Marshall, J., A. Adcroft, C. Hill, L. Perelman, and C. Heisey (1997), A finite-volume, incompressible Navier-Stokes model for studies of the ocean on parallel computers, *J. Geophys. Res.*, *102*, 5753–5766.

Martini, K., M. H. Alford, J. D. Nash, E. Kunze, and M. A. Merrifield (2007), Diagnosing a partly standing internal wave in Mamala Bay, Oahu, *Geophys. Res. Lett.*, *34*, L17,604, doi:10.1029/2007GL029,749.

Martini, K. I., M. H. Alford, S. M. Kelly, J. D. Nash, and E. Kunze (2011a), Internal tides on the oregon continental slope, in progress.

Martini, K. I., M. H. Alford, E. Kunze, J. D. Nash, and S. M. Kelly (2011b), Observations of remotely-generated internal tides breaking on the oregon continental slope, in progress.

Moum, J. N., and J. D. Nash (2008), Seafloor pressure measurements of nonlinear internal waves, *J. Phys. Oceanogr.*, *38*, 481–491.

Moum, J. N., D. Caldwell, J. D. Nash, and G. Gunderson (2002), Observations of boundary mixing over the continental slope, *J. Phys. Oceanogr.*, *32*, 2113–2130.

Muller, C., and O. Bühler (2009), Saturation of the internal tides and induced mixing in the abyssal ocean, *J. Phys. Oceanogr.*, *39*, 2077–2096.

M uller, P., G. Holloway, F. Henyey, and N. Pomphrey (1986), Nonlinear interactions among internal gravity waves, *Rev. Geophys.*, *24*, 493–536.

Munk, W. (1966), Abyssal recipes, *Deep Sea Res.*, *13*, 707–730.

Munk, W. (1968), Once again: tidal friction, *Q. J. R. Astro. Soc.*, *9*, 352–375.

Munk, W. (1981), Internal waves and small scale processes, in *Evolution of physical oceanography: Scientific Surveys in honor of Henry Stommel*, edited by B. A. Warren and C. Wunsch, pp. 264–291, The MIT Press.

Munk, W., and C. Wunsch (1998), Abyssal recipes II: energetics of tidal and wind mixing, *Deep Sea Res.*, *45*, 1977–2010.

Nansen, F. (1902), Oceanography of the North Pole Basin: Norwegian North Polar Expedition, 18931896, *Sci. Results*, *3*, 1–427.

Nash, J. D., E. Kunze, J. M. Toole, and R. W. Schmitt (2004), Internal tide reflection and turbulent mixing on the continental slope, *J. Phys. Oceanogr.*, *34*, 1117–1134.

Nash, J. D., M. H. Alford, and E. Kunze (2005), Estimating internal wave energy fluxes in the ocean, *J. Atmos. and Ocean. Tech.*, *22*, 1551–1570.

Nash, J. D., E. Kunze, C. M. Lee, and T. B. Sanford (2006), Structure of the baroclinic tide generated at Kaena Ridge, Hawaii, *J. Phys. Oceanogr.*, *36*, 1123–1135.

Nash, J. D., M. H. Alford, E. Kunze, K. I. Martini, and S. M. Kelly (2007), Hotspots of deep ocean mixing on the Oregon continental slope, *Geophys. Res. Lett.*, *34*, L01,605, doi:10.1029/2006GL028,170.

Nash, J. D., S. M. Kelly, E. L. Shroyer, J. N. Moum, and T. F. Duda (2010), Internal tides and nonlinear internal waves on the continental shelf: Why are they so unpredictable?, in prep.

Niwa, Y., and T. Hibiya (2001), Numerical study of the spatial distribution of the M_2 internal tide in the Pacific Ocean, *J. Geophys. Res.*, *106*, 22,441–22,449.

Noble, M., B. Jones, P. Hamilton, J. Xu, G. Robertson, L. Rosenfeld, and J. Largier (2009), Cross-shelf transport into nearshore waters due to shoaling internal tides in San Pedro Bay, CA, *Cont. Shelf Res.*, *29*, 1768–1785.

Nycander, J. (2005), Generation of internal waves in the deep ocean by tides, *J. Geophys. Res.*, *110*, C10,028, doi:10.1029/2004JC002,487.

Nycander, J., J. Nilsson, K. Ds, and G. Brostrm (2007), Thermodynamic analysis of ocean circulation, *J. Phys. Oceanogr.*, *237*, 2038–2052.

Osborne, A. L., and T. L. Burch (1980), Internal solitons in the andaman sea, *Science*, *208*, 451–460.

Pedlosky, J. (2003), *Waves in the Ocean and Atmosphere*, 1 ed., 183-191 pp., Springer.

Pétrélis, F., S. G. Llewellyn Smith, and W. R. Young (2006), Tidal conversion at a submarine ridge, *J. Phys. Oceanogr*, *36*, 1053–1071.

Pettersson, O. (1907), Strumstudien vid osterions portar, *Inst. Mar. Res. Lysekil Set. Biol. Rep*, *3*.

Pettersson, O. (1930), The tidal force: A study in geophysics, *Geografiska Annaler*, *12*, 261–322.

Pineda, J. (1991), Predicatable upwelling and shoreward transport of planktonic larvae by internal tide bores, *Science*, *253*, 548–550.

Rainville, L., and R. Pinkel (2006), Propogation of low-mode internal waves through the ocean, *J. Phys. Oceanogr.*, *36*, 1220–1236.

Rainville, L., S. T. M. Johnston, G. S. Carter, M. A. Merrifield, R. Pinkel, P. F. Worcester, and B. D. Dushaw (2010), Interference pattern and propagation of the M_2 internal tide south of the Hawaiian Ridge, *J. Phys. Oceanogr.*, *40*, 311–326.

Rattray, M. (1960), On the coastal generation of internal tides, *Tellus*, *12*, 5462.

Ray, R. D., and D. Cartwright (2001), Estimates of internal tide energy fluxes from TOPEX/Poseidon altimetry: Central North Pacific, *Geophys. Res. Lett.*, *28*, 1259–1262.

Ray, R. D., and G. T. Mitchum (1996), Surface manifestation of internal tides generated near Hawaii, *Geophys. Res. Lett.*, *23*, 2101–2104.

Robinson (1969), The effects of a barrier on internal waves, *Deep Sea Res*, p. 421429.

Romsos, C. G., C. Goldfinger, R. Robison, R. L. Milstein, J. D. Chaytor, and W. W. Wakefield (2007), Development of a regional seafloor surficial geologic habitat map for the continental margins of Oregon and Washington, USA, in *Marine Geological and Benthic Habitat Mapping*, edited by B. Todd and H. Greene, p. Pap. 47, Geol. Assoc. Can. Spec.

Rudnick, D. L., et al. (2003), From tides to mixing along the Hawaiian Ridge, *Science*, *301*, 355–357.

Samelson, R. M. (1998), Large-scale circulation with locally enhanced vertical mixing, *J. Phys. Oceanogr.*, *28*, 712726.

Sandstrom, H. (1976), On topographic generation and coupling of internal waves, *Geophys. Fluid Dyn.*, *7*, 231–270.

Sandström, J. W. (1908), Dynamische versuche mit meerwasser, *Ann. Hydrodynam. Mar. Meteor.*

Savidge, D. K., C. R. Edwards, and M. Santana (2007), Baroclinic effects and tides on the Cape Hatteras continental shelf, *J. Geophys. Res.*, *112*, C09,016, doi:10.1029/2006JC003,832.

Sharples, J., C. M. Moore, A. E. Hickman, P. M. Holligan, J. F. Tweddle, M. R. Palmer, and J. H. Simpson (2009), Internal tide mixing as a control on continental margin ecosystems, *Geophys. Res. Lett.*, *36*, L23,603, doi:10.1029/2009GL040,683.

Shchepetkin, A. F., and J. C. McWilliams (2005), The regional oceanic modeling system (ROMS): a split-explicit, free-surface, topography-following-coordinate oceanic model, *Ocean Modelling*, *9*, 347–404.

Sherwin, T. J., V. I. Vlasenko, N. Stashchuk, D. R. Jeans, and B. Jones (2002), Along-slope generation as an explanation for some unusually large internal tides, *Deep-Sea Res. I*, *49*, 1787–1799.

Shroyer, E. L., J. N. Moum, and J. D. Nash (2010), Vertical heat flux and lateral transport in nonlinear internal waves, *Geophys. Res. Lett.*, *37*, L08,601, doi:10.1029/2010GL042,715.

Simmons, H. L., R. W. Hallberg, and B. K. Arbic (2004), Internal wave generation in a global baroclinic tide model, *Deep-Sea Res. II*, *51*, 3043–3068.

Slinn, D. N., and J. J. Riley (1998), Turbulent dynamics of a critically reflecting internal gravity wave, *Theor. Comp. Fluid Dyn.*, *11*, 281–303.

Smyth, W. D., J. N. Moum, and J. D. Nash (2010), Narrowband, high-frequency oscillations at the equator. Part II: Properties of shear instabilities, *J. Phys. Oceanogr.*, submitted.

St. Laurent, L., and C. Garrett (2002), The role of internal tides in mixing the deep ocean, *J. Phys. Oceanogr.*, *32*, 28822899.

St. Laurent, L., J. M. Toole, and R. W. Schmitt (2001), Buoyancy forcing by turbulence above rough topography in the abyssal Brazil Basin, *J. Phys. Oceanogr.*, *31*, 34763495.

St. Laurent, L., S. Stringer, C. Garrett, and D. Perrault-Joncas (2003), The generation of internal tides at abrupt topography, *Deep-Sea Res. I*, *50*, 987–1003.

Street, R. O. (1917), The dissipation of energy in the tides in connection with the acceleration of the Moons mean motion, *Proc. Roy. Soc. London*, *93*, 348359.

Tang, W., and T. Peacock (2010), Lagrangian coherent structures and internal wave attractors, *CHAOS*, *20*, 017,508, doi:10.1063/1.3273,054.

Taylor, G. I. (1919), Tidal friction in the Irish Sea, *Phil. Trans. Roy. Soc.*, *220*, 1–33.

van Haren, H. (2004), Incoherent internal tidal currents in the deep ocean, *Ocean Dynamics*, *54*, 66–76.

Winters, K. B., and J. J. Riley (1992), Instability of internal waves near a critical level, *Dyn. Atmos. Oceans*, *16*, 249–278.

Wunsch, C. (1968), On the propagation of internal waves up a slope, *Deep-Sea Res.*, *25*, 251–258.

Wunsch, C. (1969), Progressive internal waves on slopes, *J. Fluid Mech.*, *35*, 131–144.

Wunsch, C. (1975), Internal tides in the ocean, *Reviews of Geophysics and Space Physics*, *13*, 167–182.

Wunsch, C., and R. Ferrari (2004), Vertical mixing, energy, and the general ciruclation of the ocean, *Annu. Rev. Fluid Mech.*, *28*, 281314.

Zeilon, N. (1912), On tidal boundary-waves and related hydrodynamical problems, *Kung. Svenska Vetenskapsakad. Handl.*, *4*.

Zhao, Z., and M. H. Alford (2009), New altimetric estimates of mode-1 M_2 internal tides in the central North Pcific Ocean, *J. Phys. Oceanogr.*, *39*, 1669–1684.

Zhao, Z., M. H. Alford, J. A. MacKinnon, and R. Pinkel (2010), Long-range propagation of the semidiurnal internal tide from the Hawaiian Ridge, *J. Phys. Oceanogr.*, *40*, 713–736.

Zilberman, N. V., J. M. Becker, M. A. Merrifield, and G. S. Carter (2009), Model estimates of M2 internal tide generation over Mid-Atlantic Ridge topography, *J. Phys. Oceanogr.*, *39*, 2635–2651.